Geomechanical Interpretation of Induced Seismicity at the Preston New Road PNR-2 Well, Lancashire, England

April 2020

Report Commissioned by the Oil and Gas Authority, London

Report Internal ID: OLG.OGA-PNR3

Authors:
Dr. James Verdon, Lead Geophysicist, Outer Limits Geophysics LLP
Mr Tom Kettlety, Contract Geophysicist, Outer Limits Geophysics LLP

Professor Michael Kendall, Lead Geophysicist, Outer Limits Geophysics LLP

SUMMARY

- This report analyses and interprets microseismicity and induced seismicity recorded during hydraulic fracturing at the PNR-2 well, Lancashire, in August 2019, with a focus on understanding the causative mechanisms for the M_L 2.9 event that was widely felt in the local area. This report follows on from a similar study performed for the PNR-1z microseismicity (Verdon et al., 2019a).

- The microseismicity reveals that the early stages of injection created a large hydraulic fracture system extending both northwards and southwards from the well. This fracture system interacted with several natural structures, but did not produce significant magnitudes of seismicity.

- As injection stages proceeded along the well, a second zone of hydraulic fractures began to propagate, located approximately 100 m to the east of the active sleeves. This zone intersected with a pre-existing near-vertical fault with a SE strike. This fault was responsible for the largest events, and it is clearly delineated by the aftershocks of the M_L 2.9 event.

- The fault responsible for larger PNR-2 events is a different structure to that responsible for the seismicity during stimulation of PNR-1z. There is almost no overlap between the microseismic event populations from the two wells.

- The spatio-temporal evolution of events shows a clear relationship between event distance (from the injection point) and occurrence time that is indicative of a pore pressure diffusion-driven process. This is different to the PNR-1z case, where events occurred across a range of distances nearly instantaneously, which was taken by Verdon et al. (2019a) to be indicative of a static stress transfer process. The diffusion process means that many of the large events occurred after injection, as there was a time delay for elevated pore pressures to reach the seismogenic region.

- While pressure diffusion appears to play a dominant role for the PNR-2 microseismicity, we also model the stress transfer effects produced by tensile fracture opening, finding that these effects would also have acted to promote slip on the fault. Therefore, multiple factors may have contributed to the triggering of the seismicity.

- We compare the reactivation of the two different faults during PNR-1z and PNR-2 stimulation. The PNR-1z fault received a higher volume of injected fluid, and yet produced less seismicity. We compare the orientations of the faults within the *in situ* stress field, finding that the PNR-1z fault is moderately well orientated for slip, whereas the PNR-2 fault is extremely well orientated for slip. Hence, the stress conditions, and the fault orientation within the stress field, appears to have a significant impact on the magnitudes of earthquakes that result.

DISCLAIMER

Forecasts, projections and forward-looking statements contained in this presentation are derived from geophysical modelling based on a range of parameters that are not necessarily well constrained. Therefore the nature of this work entails a number of risks, uncertainties or assumptions. Hence, no representation or warranty is given as to the achievement or reasonableness of any projections, estimates, forecasts or forward-looking statements contained in this presentation.

3rd party information contained in the presentation is believed to be accurate. However, the authors disclaim any liability if such information is found to be inaccurate.

The dissemination of this presentation nor its contents is to be taken as any form of commitment on the part of the author to enter any contract or otherwise legally binding obligation or commitment. The authors expressly reserve the right without prior notice or liability to terminate discussions with any recipient or other parties.

1. INTRODUCTION

This report provides a geomechanical interpretation of microseismicity and induced seismicity generated by hydraulic fracturing of the Preston New Road PNR-2 well, situated on the Fylde Peninsula, Lancashire, in August 2019. The well was operated by Cuadrilla Resources Ltd. (CRL). During this operation, an earthquake with magnitude M_L 2.9 was generated by the hydraulic stimulation. This event was felt by the public across the local area. In response to this event, the hydraulic fracturing operation was stopped, and no further activities have taken place at the site. This report follows on from a similar study performed by Outer Limits for the adjacent PNR-1z well, which was stimulated in late 2018, producing an M_L 1.5 event, which was felt by a few nearby residents in close proximity to the site (Verdon et al., 2019a).

Induced seismicity occurs when hydraulic fractures interact with and reactivate pre-existing faults in the subsurface (e.g., Maxwell et al., 2008; Maxwell et al., 2009; Kettlety et al., 2019; Verdon et al., 2019b; Eyre et al., 2019, Clarke et al., 2019a). However, all hydraulic fracturing produces very low magnitude "microseismic" events, with magnitudes typically being less than $M < 0$, which is far too small to be felt at the surface. This is sometimes referred to as operationally-induced microseismicity (Eaton, 2018). These microseismic events can be detected and located by arrays of geophones placed in boreholes near to the reservoir. Their locations can be used to map and understand the propagation of hydraulic fractures in the subsurface, and their interactions with pre-existing structures such as faults. Monitoring of this kind was conducted during stimulation of the PNR-1z and PNR-2 wells. In both cases, tens of thousands of recorded microseismic events provided a detailed and high-resolution view of the geomechanical processes that occurred during hydraulic stimulation.

1.1. MECHANISMS FOR FAULT REACTIVATION DURING HYDRAULIC FRACTURING

Processes that lead to fault reactivation during subsurface fluid injection are typically considered with respect to their impact on the stress conditions in the rock mass. For a given fault, the stress field can be resolved into normal (σ_n) and shear (τ) stresses. The Mohr-Coulomb failure envelope describes the conditions at which fault slip will begin to occur:

$$\tau > m(\sigma_n - P) + C, \tag{1.1}$$

where P is the pore pressure, m is the friction coefficient and C is the cohesion. The proximity of the *in situ* stress state to the Mohr Coulomb threshold can be re-written in terms of the Coulomb Failure Stress, *CFS*:

$$CFS = \tau - m(\sigma_n - P). \tag{1.2}$$

If a process causes a change in *CFS*, noted hereafter as ΔCFS, then it will move the fault towards the failure threshold, increasing the likelihood of seismicity occurring.

Subsurface injection will always cause an increase in pore pressure, since additional fluid is added into the system. Equation 1.2 shows that this will increase *CFS*, promoting faults to slip. Hence pore pressure increases associated with injection are typically considered to be the driving mechanism for injection-induced seismicity (e.g., Holland et al., 2013; Schultz et al., 2015; Verdon et al., 2019b).

Subsurface fluid injection will also create geomechanical deformation as the rock mass expands in a poroelastic manner (e.g., Rice and Cleary, 1976). This expansion will affect the stress field in the surrounding rocks. The impact this deformation has on σ_n or τ acting on a nearby fault will depend on the relative orientations and positions of both the fault in question and the poroelastic deformation. If it either decreases σ_n or increases τ (or does both) then it will promote slip, and potentially cause induced seismicity (e.g., Deng et al., 2016; Bao and Eaton, 2016; Kettlety et al., 2020). Stress transfer effects have been shown to control the positions of aftershock events after a large earthquake (e.g., Stein, 1999), and of earthquakes associated with magma movement in volcanic settings (e.g., Toda et al., 2002; Green et al., 2015).

Transfer of pore pressure perturbations through the rock pore space, from the injection point to the reactivated fault, requires time (often hours or days); whereas transfer of stress through the rock frame takes place instantaneously (or at least at the speed of a compressional wave, i.e. thousands of m/s). Hence, event occurrences at a range of distances from an injection point within a short space of time might indicate events triggered by stress transfer, whereas a progression of events at increasing distances with time might indicate a process dominated by pore pressure diffusion (e.g., Shapiro et al., 1997; Shapiro, 2008; Shapiro and Dinske, 2009).

During stimulation of the PNR-1z well, Verdon et al. (2019a) observed microseismic events occurring at a range of distances from the well, with little temporal evolution of event positions. Moreover, we simulated the stress perturbations that would be produced by the tensile opening of hydraulic fractures and found that a significant majority of events occurred in regions that would have experienced positive ΔCFS changes, while microseismicity may have been suppressed in regions that experienced negative ΔCFS changes. This led us to conclude that the microseismicity observed during the PNR-1z stimulation was driven by static stress transfer effects.

In the following chapters we perform a similar analysis for the PNR-2 microseismicity. In Chapter 2 we provide a brief re-cap of the monitoring system. In Chapter 3 we describe the microseismicity as it occurred during each stage, showing how it imaged the hydraulic fractures created during the stimulation, and illuminated the re-activated fault responsible for the larger-magnitude events, as well as other pre-existing structures within the reservoir. In Chapter 4 we analyse the frequency-magnitude distributions of the event population, using these observations to further characterise the deformation processes. In Chapter 5 we examine the spatio-temporal evolution of the microseismicity in more detail, using this to characterise possible triggering processes. In Chapter 6 we model the poroelastic stress changes produced by the hydraulic fracturing, and assess whether they would have promoted slip on the identified fault. In Chapter 7 we compare the seismic response produced by the faults reactivated by stimulation of both the PNR-1z and PNR-2 wells, focussing on their orientations within the stress field as a key factor in explaining the differences in their responses.

2. MICROSEISMIC MONITORING AT PNR-2

A surface monitoring array and a downhole geophone array were used in combination to monitor the microseismicity at the Preston New Road site. Both arrays provided real-time data to the operator. In this study we use the event catalogues provided by the operator to the OGA, without performing any re-analysis of event locations.

2.1. SURFACE ARRAY

The primary objective of the surface monitoring array was to provide accurate local magnitudes for larger events ($M_L \geq 0$) in order to administer the Traffic Light Scheme (TLS). The array consisted of broadband seismometers and geophones deployed by CRL, augmented by seismometers deployed by the British Geological Survey (BGS). During real-time monitoring, the surface array detected over 120 events with a minimum magnitude of $M_L = -1.7$. The aperture of the surface array was sufficient to enable focal mechanisms to be determined for many of the larger events.

2.2. DOWNHOLE ARRAY

Surface arrays are limited in their event detection capability by the relatively high levels of noise at the surface, and by the fact that they are separated from the events by kilometres of overburden rock. Geophones installed in boreholes near to the reservoir can therefore provide a significant improvement in event detection. The microseismicity at PNR-2 was monitored with an array of 12 geophones placed in the build section (i.e., the section where the well deviates from vertical to horizontal) of the nearby PNR-2 well (Figure 2.2). This array reported over 55,000 events during real-time monitoring with a minimum magnitude of $M_W = -2.6$. The proximity of the downhole array to the events also means that it provided more precise event locations than the surface array (Kettlety et al., 2020). We therefore use the downhole event locations in the following chapters.

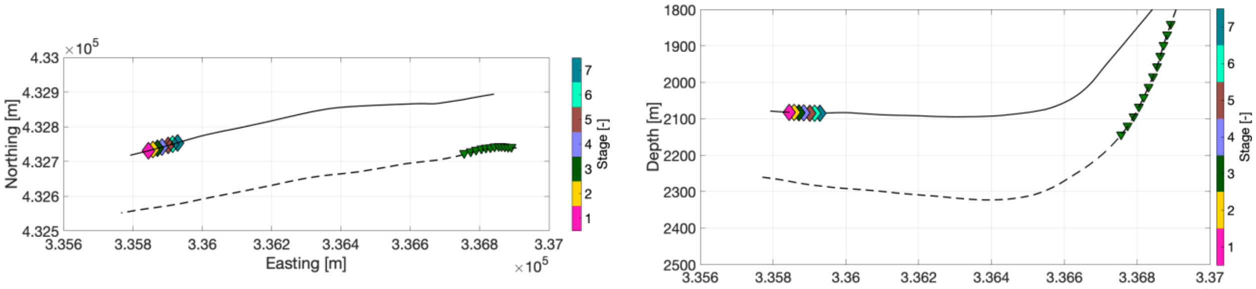

(a)

(b)

Figure 2.2. Map (a) and cross-section (b) showing the downhole microseismic monitoring array deployed in the PNR-1z well (green triangles) and the injection sleeves in the PNR-2 well (diamonds, coloured by sleeve number from toe to heel).

2.3. MAGNITUDE SCALES

The downhole array reported moment magnitudes, M_W (Hanks and Kanamori, 1979), whereas the surface array reported local magnitude, M_L, using the UK local magnitude scale adapted for short hypocentral distances (Butcher et al., 2017; Luckett et al., 2019). The moment and local magnitude scales diverge at low magnitudes. In this report we use the surface-based M_L scale when discussing the felt events, to ensure consistency with event reports issued publicly by the BGS. However, in all plots and analysis we use M_W values, where the surface array M_L values are converted to M_W using the relationship:

$$M_W = 0.651 M_L + 0.901 \ . \tag{2.1}$$

We note that M_W scales should be used when making assessments of fault rupture dimensions, and, for example, when linking seismic moment release to injected volumes to make magnitude forecasts (e.g., Clarke et al., 2019a). Equation 2.1 means that the largest event, which had a local magnitude of M_L 2.9, has a moment magnitude of M_W 2.8. However, smaller events have higher values for M_W than they do for M_L: for example, the M_L 1.6 event that occurred after Stage 6 has an M_W of 1.9. This relationship, $M_W \approx 2/3\ M_L$, is commonly observed for small-magnitude earthquakes (e.g., Deichmann 2006; Butcher et al., 2020).

3. MICROSEISMIC OBSERVATIONS AND IDENTIFICATION OF FAULTS

The PNR-2 well extends laterally over approximately 700 m through the Upper Bowland Shale formation. A sliding sleeve completion method was used, with injection ports that can be opened and closed as required. A total of 47 such ports were installed, spaced at 14 m. Each stage was expected to inject approximately 400 m^3 of water, and up to 75 tonnes of proppant (Cuadrilla Resources, 2019). Of the 47 planned stages, 7 were completed before the occurrence of the M_L 2.9 event, starting at the toe of the well and moving eastwards along it.

3.1. MICROSEISMICITY TIMELINE

Figure 3.1 shows the timeline of microseismicity during stimulation of the PNR-2 well. After initial mini-frac tests on the 13th and 14th August, the first 5 stages were conducted between the 15th – 20th August, without any red-light $M_L \geq 0.5$ events. Stage 6 was injected on the 21st August. No events with $M_L \geq 0.5$ occurred during injection, but several hours afterwards an M_L 1.6 event occurred, followed by an M_L 1.0 event the next day. These events triggered the TLS red light, requiring a pause in operations of at least 18 hours.

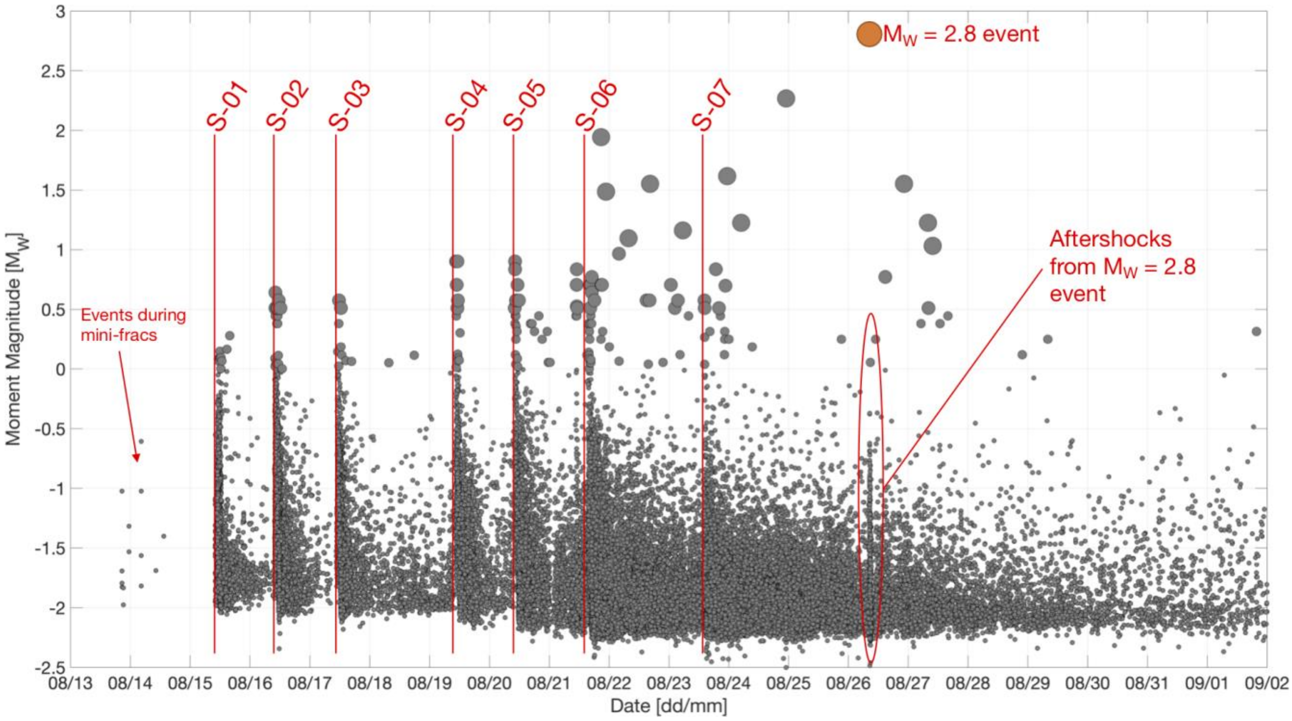

Figure 3.1: Timeline of seismicity at PNR-2. Each stage was accompanied by a burst of events. The first significant levels of seismicity were observed following Stage 6, while the $M_W = 2.8$ event occurred more than 48 hours after injection into Stage 7.

Stage 7 was injected on the 23rd August. Much like Stage 6, no $M_L \geq 0.5$ events occurred during injection. However, levels of seismicity again began to increase several hours after injection, with an M_L 1.1 event during the evening of August 23rd, followed by an M_L 2.1 event on the 24th August, and the M_L 2.9 event occurring at 08:30 on the 26th August, 3 days post injection. After this event, levels of seismicity began to subside – while 25 further events were detected by the surface array after the *ML* 2.9 event, the largest had *ML* 0.2, and only 3 had magnitudes larger than *ML* 0.0. The downhole array was demobilised at the end of September when further operations at the PNR site were officially suspended, while the last event to be recorded by the surface array occurred on the 6th October.

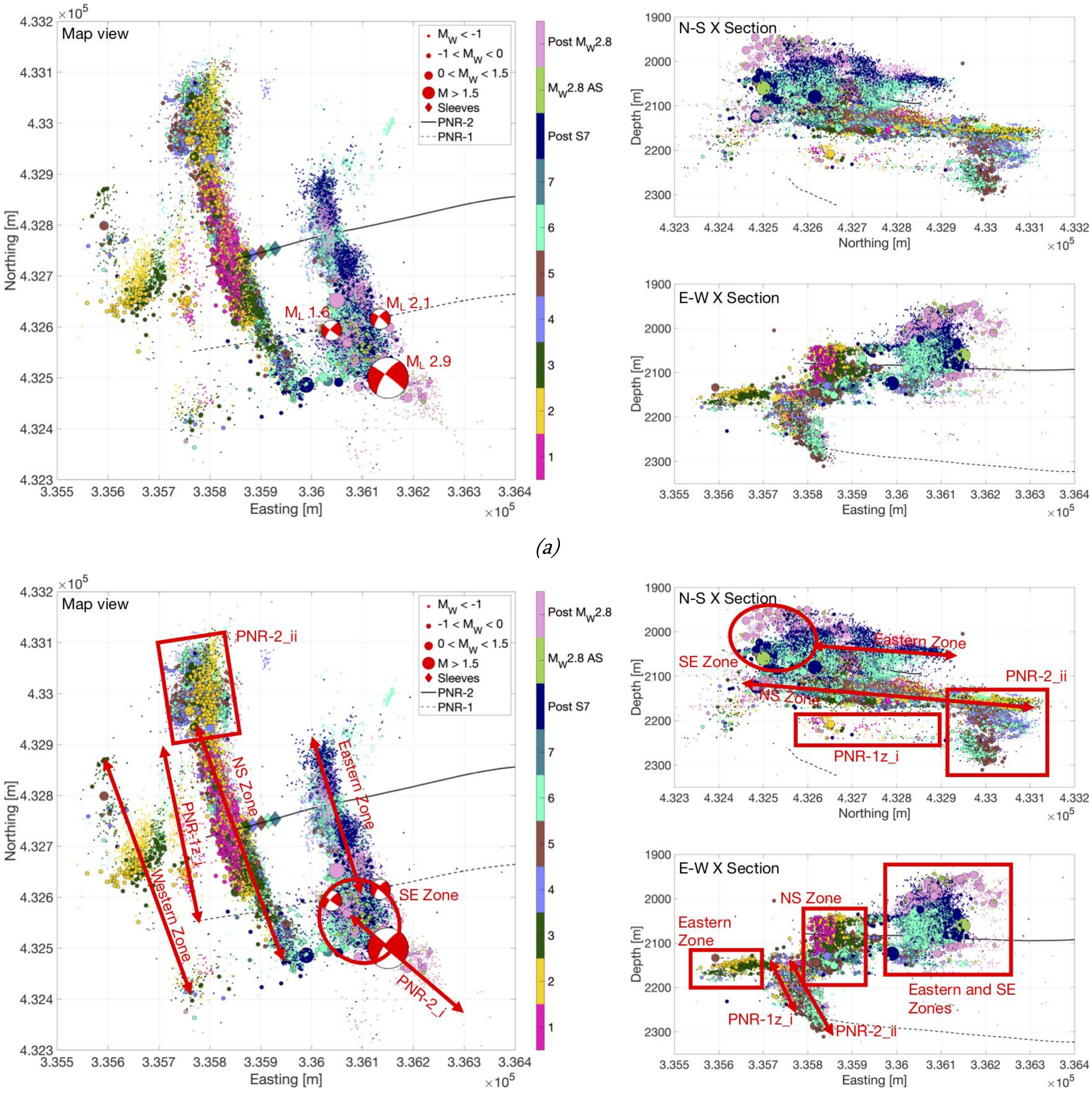

(a)

(b)

Figure 3.2: Map and cross sections showing the locations of all microseismic events recorded during stimulation of the PNR-2 well. Events are sized by magnitude, and coloured by stage number, with Post S7 denoting events that occurred from the evening of the 23rd August until the Mw 2.8 event at 08:30 on 26th August; Mw 2.8 AS denoting the aftershocks from this event until 09:30 on the 26th; and Post Mw 2.8 denoting events after 09:30 on the 26th. The solid black line shows the PNR-2 well, and the dashed line shows the PNR-1z well. The injection sleeves are shown by diamonds, coloured by stage number. Focal mechanisms for the ML 1.6, ML 2.1, and ML 2.9 events are

shown in the map view panels. In (b) we show the same data, but with annotations showing the key features as discussed in the text.

3.2. STRUCTURES ILLUMINATED BY THE MICROSEISMICITY

Figure 3.2 shows a map and cross-sections of all microseismic events that occurred during hydraulic fracturing of the PNR-2 well, highlighting several key structures that were illuminated by the microseismicity. Figures 3.3 – 3.12 shows the spatio-temporal evolution of the microseismicity during each stage. In the following pages we describe the key observations made during each stage.

Stage 1

During Stage 1, most of the microseismicity formed a cluster extending approximately 150 m to the north and south, centred on the injection point. The orientation of this cluster is NNW-SSE, with a strike of approximately 170°, This is parallel to the orientation of the maximum horizontal stress, θ_{SHMAX} = 173°, at this site (Clarke et al., 2019b), and is also consistent with the observed orientation of hydraulic fracture growth at the PNR-1z well (Kettlety et al., 2020). No events exceeded magnitude M_L 0.0, and the Gutenberg and Richter (1944) b value for these events (G-R hereafter) was high (see Chapter 4), which is indicative of events directly associated with hydraulic fracture propagation (e.g., Verdon et al., 2013; Kettlety et al., 2019). We therefore interpret this event cluster as representing hydraulic fracture growth from the PNR-2 well, parallel to the θ_{SHMAX} direction, extending approximately 150 m from the well. We refer to this cluster as the NS Zone hereafter.

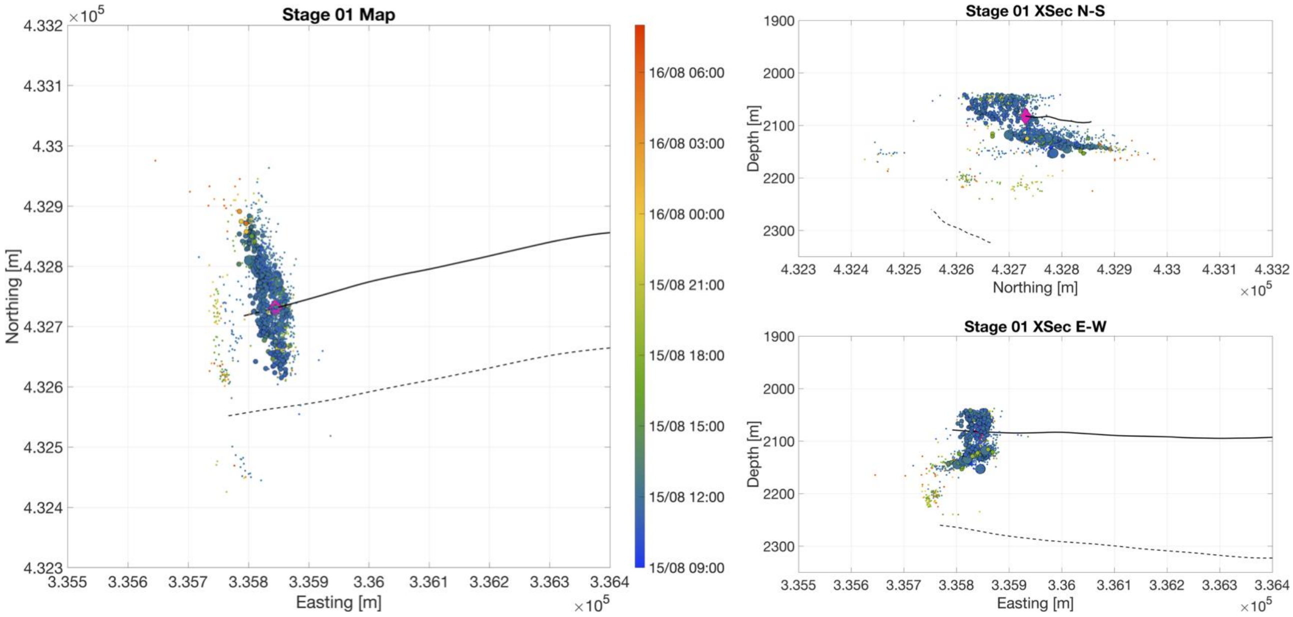

Figure 3.3: Map and cross sections of events during Stage 1. Events are coloured by occurrence time (colourbar units are dd/mm, HH:MM), and sized by magnitude (see Figure 3.2 for legend).

In addition to the main NS Zone, a small number of low-magnitude events occurred on a feature further to the west, offset by approximately 70 m to the west, and 100 m below the injection point. This feature has a roughly north-south strike, and dips steeply to the east. It is in alignment with a structure identified during stimulation of the PNR-1z well, termed PNR-1z_i by Cuadrilla Resources (2019), although the events observed during PNR-2 are shallower than those from PNR-1z and there is no overlap in events between the two populations (see Section 3.3). Nevertheless, these events could represent a reactivation of the same structure. This structure did not produce high magnitude events during stimulation of either well.

Stage 2

Microseismicity during Stage 2 occurred primarily along the same NS Zone described above, extending the zone of hydraulic fracturing to approximately 350 m to the north of the well, and 250 m to the south of the well. Event magnitudes increased slightly from Stage 1, though all were below M_L 0.0. Events again occurred along the PNR-1z_i structure below and to the west of the well. In addition, another structure began to develop, further to the west of the PNR-1z_i structure, and slightly below the well. This event cluster is slightly more diffuse than the main NS Zone, although it is consistent with the orientation of θ_{SHMAX}. It also has a high G-R *b* value (see Chapter 4), indicative of events that are directly associated with hydraulic fracturing. We refer to this cluster hereafter as the “Western Zone”. Our preferred interpretation is that it delineates a second zone of hydraulic fracture propagation, offset to the west of the well. The gap between Western Zone hydraulic fracture growth and the point of injection could be the result of a stress shadow forming from the opening of fractures in the central NS Zone. This is explored further in Chapter 6.

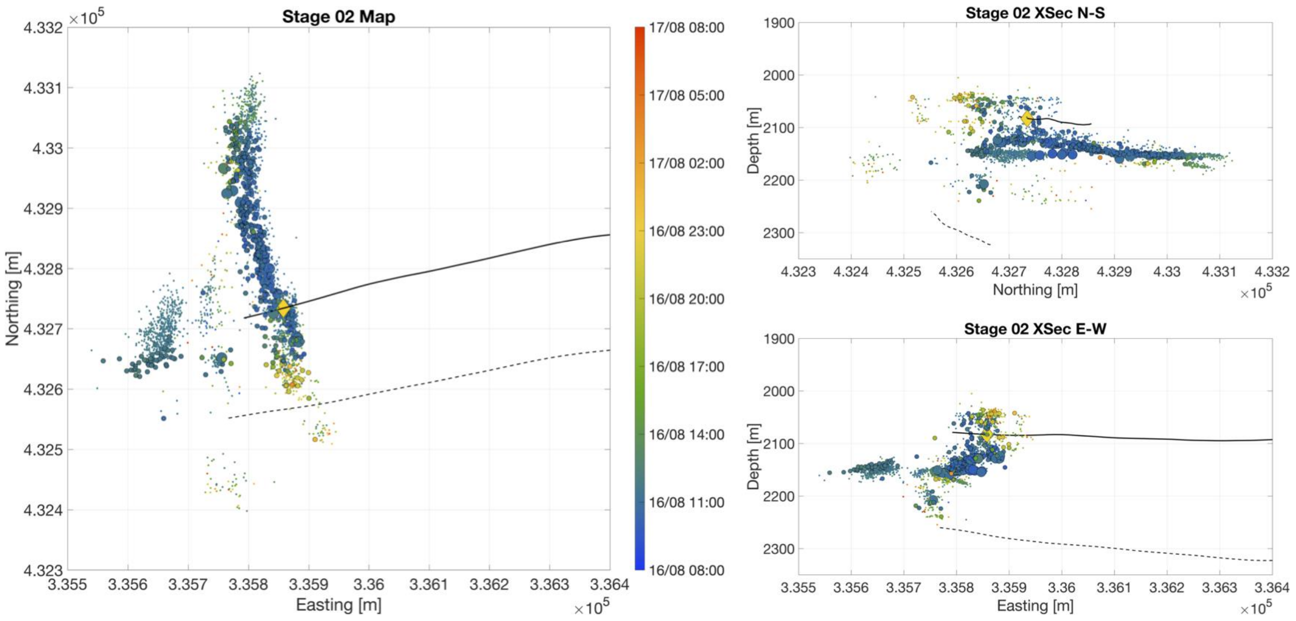

Figure 3.4: Map and cross sections of events during Stage 2. Events are coloured by occurrence time and sized by magnitude (see Figure 3.2 for legend).

Stage 3

Events during Stage 3 showed a similar distribution to the Stage 2 events. The bulk of the microseismicity was within the main NS Zone, indicating further hydraulic fracture propagation within this area, with smaller numbers of events occurring in the PNR-1z_i and Western Zone features to the west of the well.

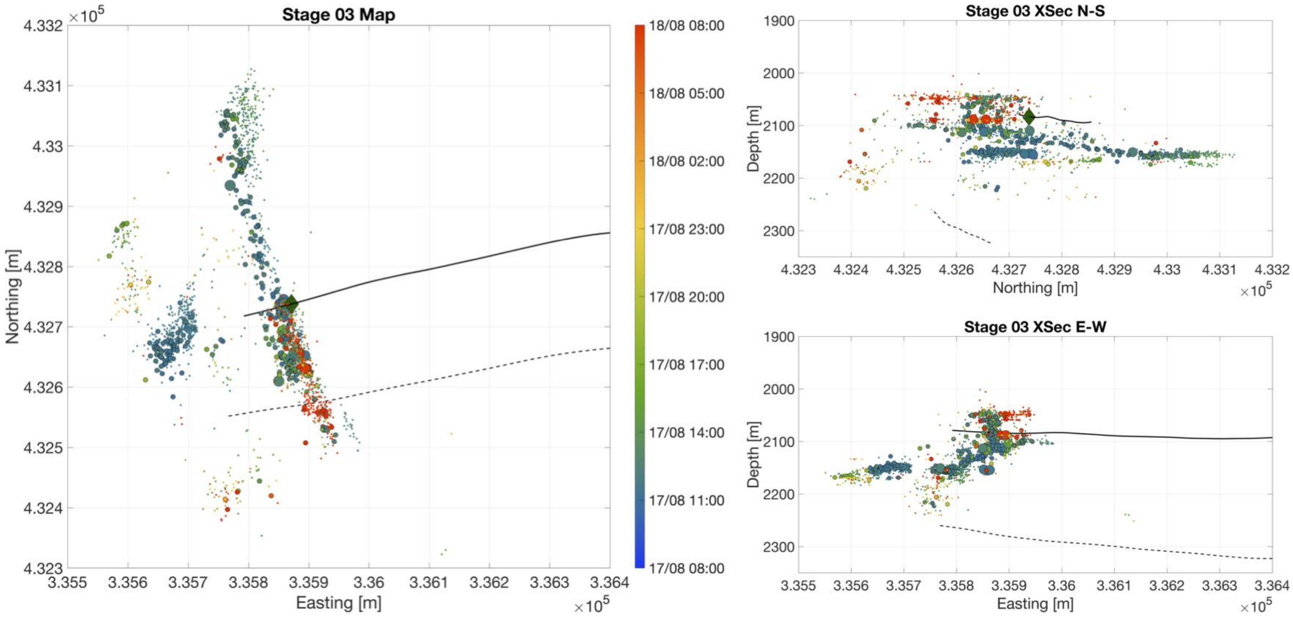

Figure 3.5: Map and cross sections of events during Stage 3. Events are coloured by occurrence time and sized by magnitude (see Figure 3.2 for legend).

Stage 4

During Stage 4, the injection point was now located approximately 30 m to the east of the main NS Zone. Nevertheless, the majority of events were located within this feature, implying that the injected fluid was able to continue generating hydraulic fractures through the same, previously stimulated zone. However, there was minimal activity within the Western Zone and the PNR-1z_i feature to the west of the well, most likely implying that, as the point of injection moved further to the east, these regions were no longer influenced by the stimulation.

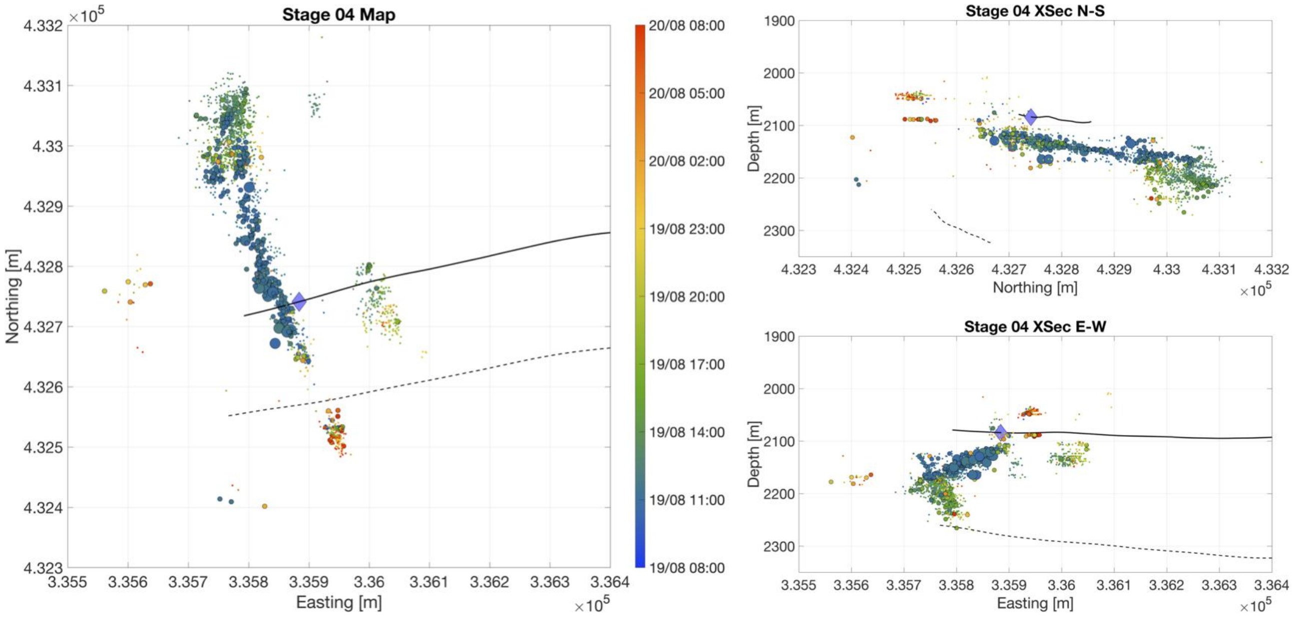

Figure 3.6: Map and cross sections of events during Stage 4. Events are coloured by occurrence time and sized by magnitude (see Figure 3.2 for legend).

At the northern tip of the main NS Zone, the microseismicity started to image a new feature that extends approximately 130 m below the depth at which the NS Zone hydraulic fractures propagated. This structure has a roughly northward strike, and dips to the east. In this respect it has a similar orientation to the PNR-1z_i feature described above, as well as other seismic discontinuities identified in the 3D reflection seismic surveys (Cuadrilla Resources, 2019). We refer to this feature as PNR-2_ii hereafter. Much like the PNR-1z_i feature, no large magnitude events occurred on PNR-2_ii, and it produced elevated G-R *b* values (see Chapter 4), indicating that microseismicity was driven directly by pore pressure and fluid flow effects, rather than the release of tectonic stress. The largest event during Stage 4 had a magnitude of M_L 0.0.

After injection of Stage 4 had stopped, events began to occur in a new zone approximately 100 m to the east of the main NS Zone, roughly at the position of Sleeve 13, and slightly deeper than the well. We refer to this hereafter as the Eastern Zone. This cluster propagates roughly 50 m southwards along the θ_{SHMAX} orientation. The orientation and growth of this feature from the well, and its elevated G-R *b* value (see Chapter 4), suggests it was a new zone of hydraulic fracture growth.

It is not clear why this zone of hydraulic fracturing initiated here, 100 m to the east of the injection stage. The possibility that the Sleeve 13 injection port was open can be ruled out immediately, because most of the microseismicity continues to occur in the main NS Zone, and events in the Eastern Zone only start to occur after the end of injection. If the Sleeve 13 port had somehow become open, then the majority of the injection, and therefore majority of the microseismicity, would take place via this point, as it is closer to the heel of the well. We investigate possible explanations for the initiation of hydraulic fracturing in the Eastern Zone in Chapter 6.

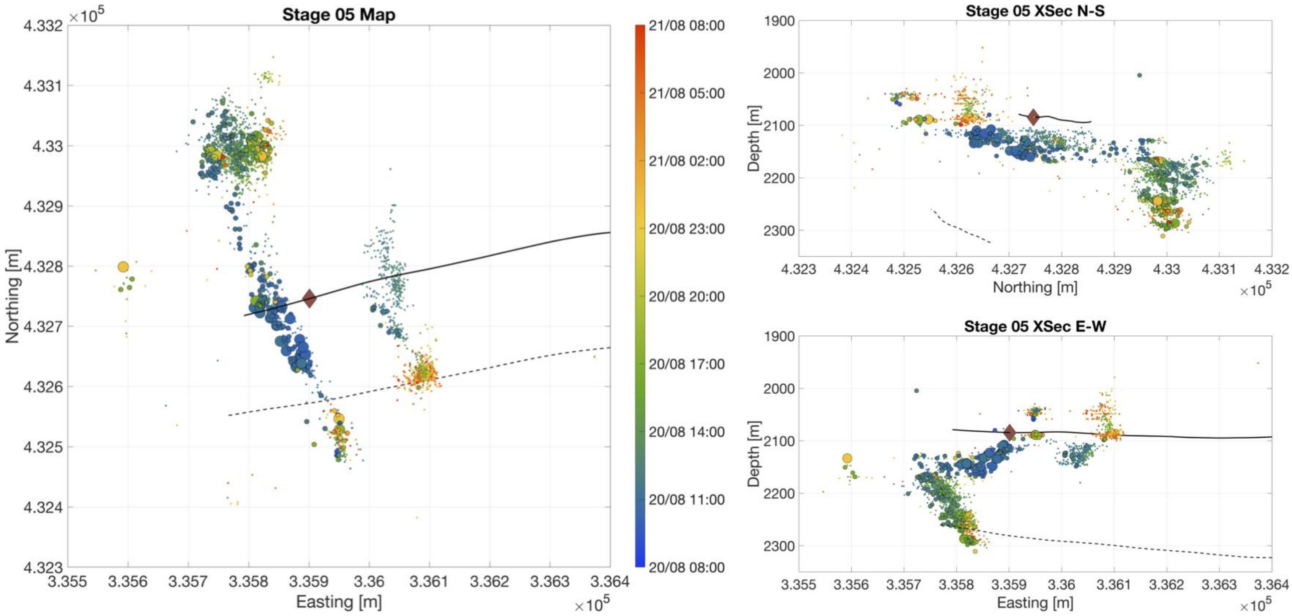

Figure 3.7: Map and cross sections of events during Stage 5. Events are coloured by occurrence time and sized by magnitude (see Figure 3.2 for legend).

Stage 5

During Stage 5, most of the microseismicity continued to occur along the NS Zone, and the eastward-dipping PNR-2_ii feature at its northern end. Microseismicity also occurred in the Eastern Zone, increasing its length to approximately 100 m both to the north and south of the well. Several hours after injection of Stage 5, further microseismicity began to occur at the southern tip of the Eastern Zone. The delayed onset of these events may reflect continued fluid pressure diffusion from the hydraulically stimulated areas, reaching a more seismogenic volume of rock in this area. We refer to this sub-cluster, at the southern tip of Eastern Zone, as the SE Zone hereafter. The largest event during Stage 5 had a magnitude of M_L 0.0.

Stage 6

The injection point for Stage 6 is roughly midway between the two main zones of hydraulic fracturing (the NS Zone and the Eastern Zone). During injection, microseismicity occurred within both zones, although more and larger events occurred in the NS Zone during injection. Events also continued to occur on the PNR-2_ii structure at its northern end. The largest event to occur during injection had a magnitude of M_L -0.3. After injection stopped, microseismicity continued to occur, both at the southern tip of the NS Zone, and in particular along the Eastern Zone, and at the SE Zone at its tip.

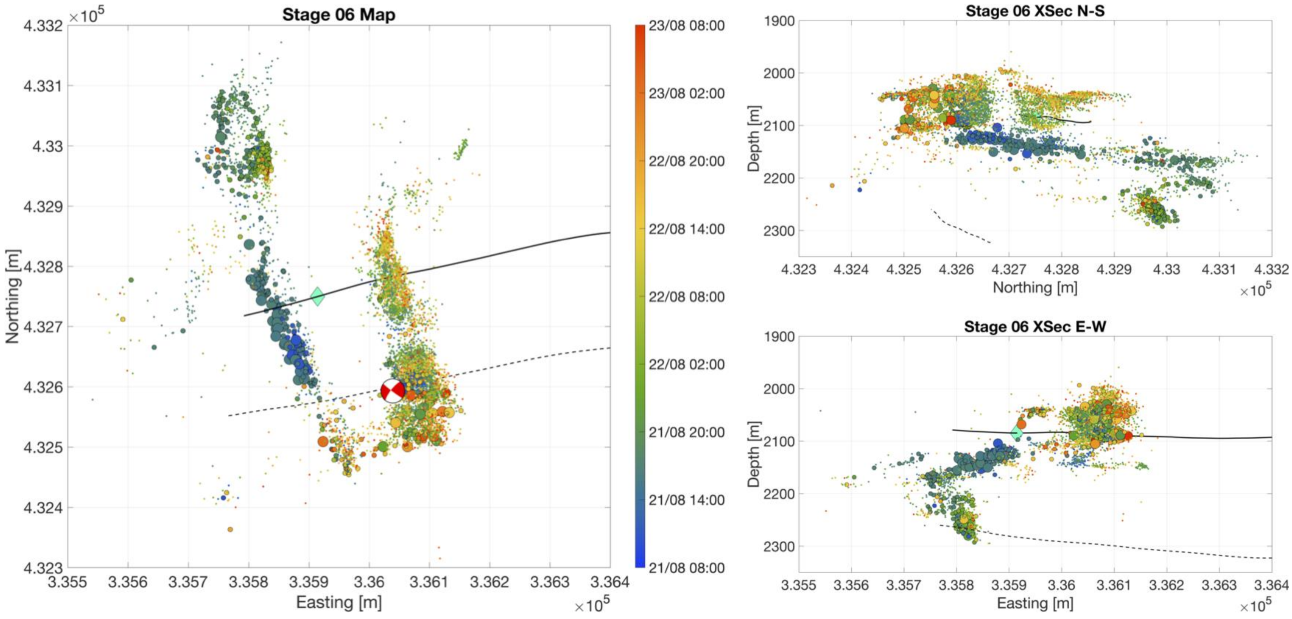

Figure 3.8: Map and cross sections of events during Stage 6. Events are coloured by occurrence time and sized by magnitude (see Figure 3.2 for legend). The focal mechanism of the M_L 1.6 event that occurred after Stage 6 is shown in map view.

Approximately 5 hours after injection, an M_L 1.6 event occurred within the SE Zone. This triggered the TLS red light, suspending any injection for at least 18 hours. During the observation period that followed, 2 more $M_L > 0.5$ events occurred, including an M_L 0.9 and an M_L 1.0, all of which were located in the SE Zone. The focal mechanism for the M_L 1.6 event, shown in Figure 3.8, indicates strike-slip motion on a near-vertical fault, with either left-lateral motion on a NE-SW striking fault, or right-lateral motion on a NW-SE striking fault. Given the locations of events in this region, it was not possible to determine the preferred slip and auxiliary planes, and both senses of motion were consistent with the regional stress field determined by Clarke et al. (2019b).

Stage 7

Stage 7 was injected on the 23rd August. The operator used a reduced volume (160 m^3) and increased the viscosity of the injection fluid. During injection, microseismic activity occurred along both the NS Zone and the Eastern Zone, indicating that injected fluid was stimulating both hydraulic fracturing zones. No events larger than $M_L > 0$ occurred during injection of Stage 7.

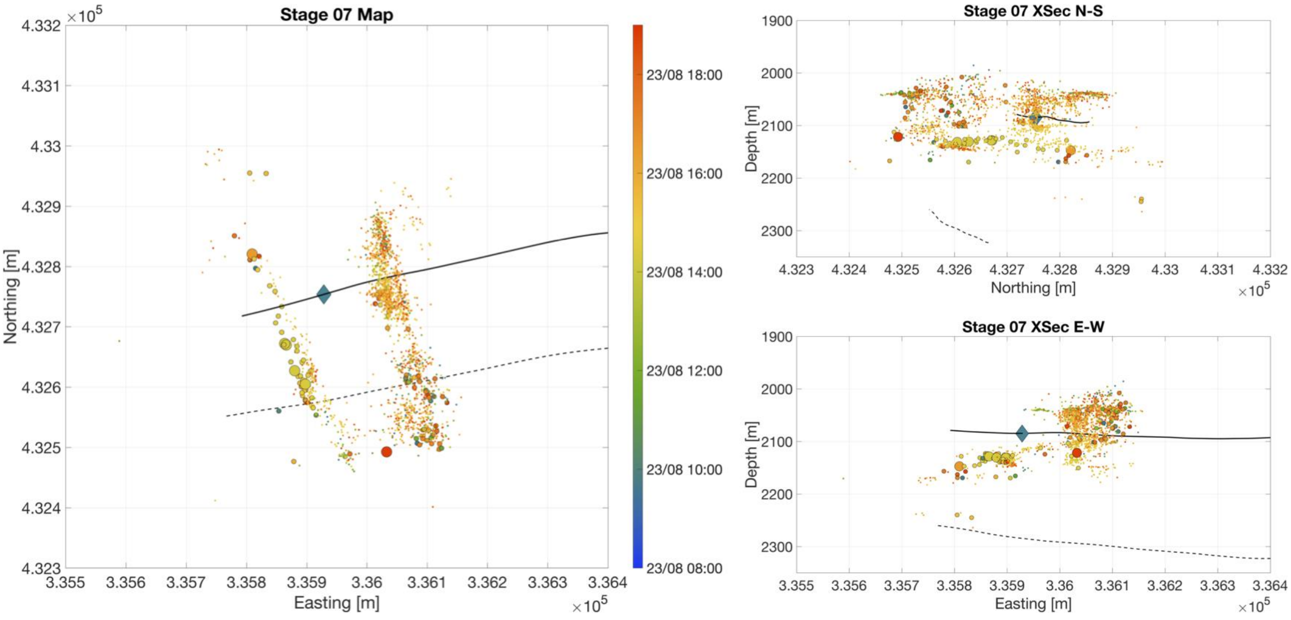

Figure 3.9: Map and cross sections of events during Stage 7. Events are coloured by occurrence time and sized by magnitude (see Figure 3.2 for legend).

Once injection had stopped, microseismicity ceased along the NS Zone and on the PNR-2_ii structure. However, it continued to occur along the Eastern Zone, and particularly in the seismogenic SE Zone at its southern end (Figure 3.10). Roughly 5 hours after the end of injection, magnitudes began to increase within this zone, with an M_L 1.1 event occurring at 23:22 on the 23rd. Seismicity continued in this zone over the next few days, with an M_L 0.5 event at 05:01 on the 24th, 14 hours after the end of Stage 7, an M_L 2.1 earthquake at 23:01 on the 24th, 33 hours after the end of Stage 7, followed by the M_L 2.9 event at 08:30 on the 26th August, more than 60 hours after the end of Stage 7.

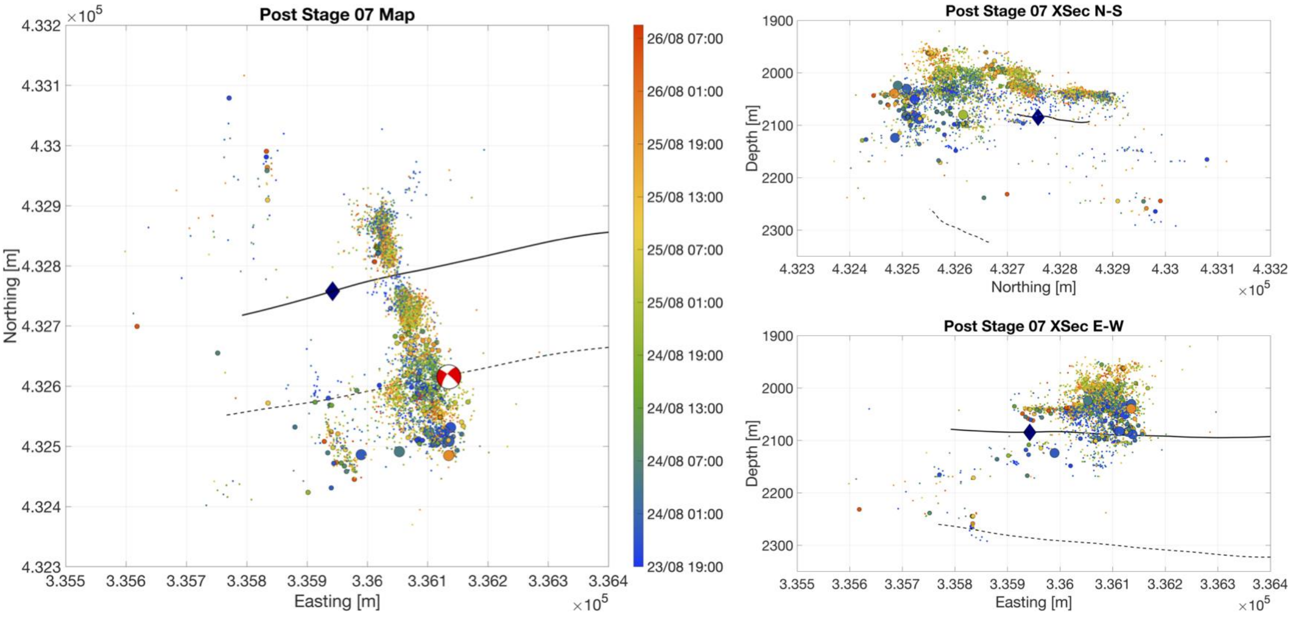

Figure 3.10: Map and cross sections of events after Stage 7 and before the M_L 2.9 event. Events are coloured by occurrence time and sized by magnitude (see Figure 3.2 for legend). The focal mechanism of the M_L 2.1 event that occurred during this period is shown in map view.

The M_L 2.9 Earthquake on 26th August

The M_L 2.9 earthquake at 08:30 on the 26th August was widely felt across the area. It was well recorded by the surface array. However, the downhole array was not recording at this time (over 60 hours since the last injection stage) due to a technical issue. This means that a location estimate is only possible from the surface data, which Kettlety et al. (2020) have shown has relatively poor precision in comparison to the downhole data. However, the downhole array was able to record a sequence of aftershocks that occurred, with microseismicity rates remaining elevated for roughly an hour after the M_L 2.9 mainshock. The largest of these immediate aftershocks had a magnitude of M_L -1.3.

We are therefore able to use the aftershock locations as determined from the downhole array to delineate the rupture surface of the M_L 2.9 event. The aftershocks are shown in Figure 3.11, and they define a near-vertical plane, extending to the southeast from SE Zone discussed above. Fitting a fault plane to these events gives a strike of 140° and a dip of 85°. This is consistent with the NW-SE striking nodal plane of the M_L 2.9 event focal mechanism, which has a strike/dip/rake of 127/84/-160°. We refer to this fault plane as PNR-2_i hereafter.

The aftershocks occurred around an elliptical zone, the centre of which was relatively quiescent. We interpret this as the aftershocks mapping a "halo" around the M_L 2.9 rupture zone, where stresses will have accumulated during the mainshock rupturing process. This interpretation can be tested by examining the dimensions of this zone, relative to that expected from an event of this size. Seismic moment, M_O, is defined by the area of rupture, A, the shear modulus μ, and the slip length d by (Aki, 1966):

$$M_O = \mu A d \ . \tag{3.1}$$

The stress drop, $\Delta\sigma$, that occurs during an earthquake can be approximated by (Kanamori and Brodsky, 2004):

$$\Delta\sigma \approx \mu \frac{d}{\sqrt{A}} \ , \tag{3.2}$$

meaning that the rupture area can be estimated from:

$$A \approx \left(\frac{M_O}{\Delta\sigma}\right)^{2/3} \ . \tag{3.3}$$

Earthquake stress drops are observed to be remarkably consistent across a wide range of magnitudes (e.g., Abercrombie, 1995), with values ranging from $0.1 < \Delta\sigma < 10$ MPa, with a typical value being $\Delta\sigma = 1$ MPa. Using this value in Equation 3.3, with the seismic moment of an M_W 2.8 event gives a rupture area of $A \approx 7.4 \times 10^4$ m^2.

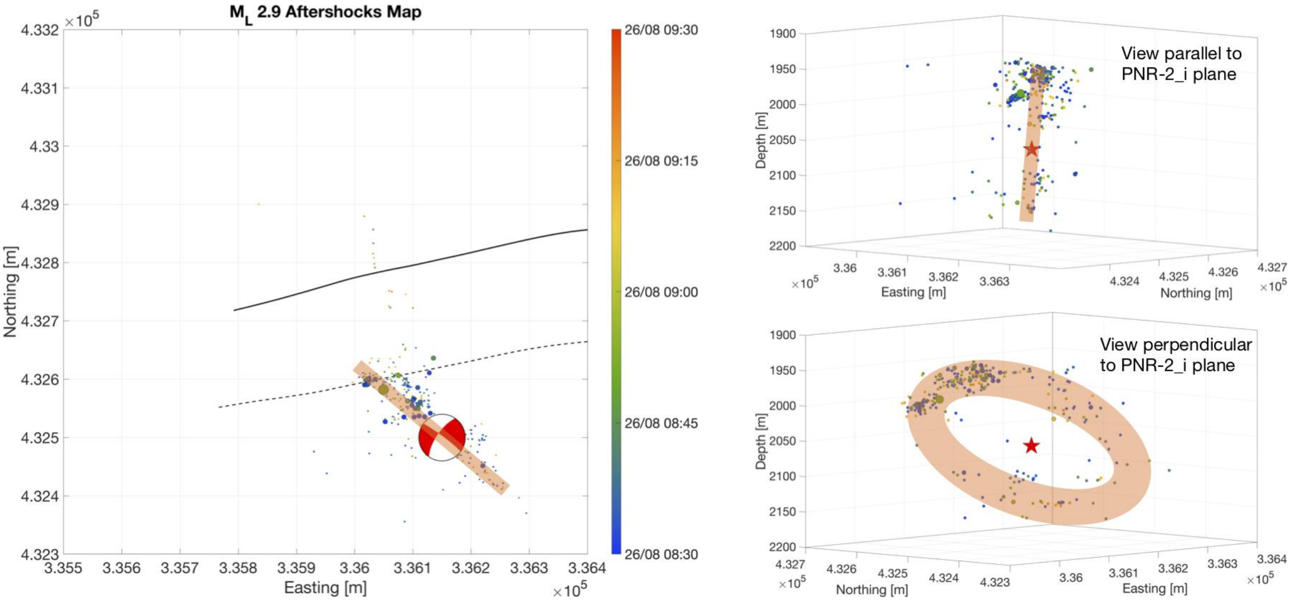

Figure 3.11: Map and 3D views of the aftershocks that occurred in 1 hour after the M_L 2.9 event. Events are coloured by occurrence time. The events define a planar structure with a strike of 140° and a dip of 85°. Within the plane, the aftershocks occur in an elliptical "halo", within which is relatively quiescent. We infer that this defines the rupture of the mainshock, and place the hypocentre of the M_L 2.9 event at the centre of this ellipse.

The dimensions of the elliptical zone in Figure 3.11 have lengths of 330 x 250 m. The area of an ellipse with such dimensions is $A \approx 6.5 \times 10^4$ m^2. Given the assumptions made about stress drop, these values can be considered equivalent, confirming that the quiescent zone ringed by aftershocks does represent the rupture area for the M_L 2.9 event.

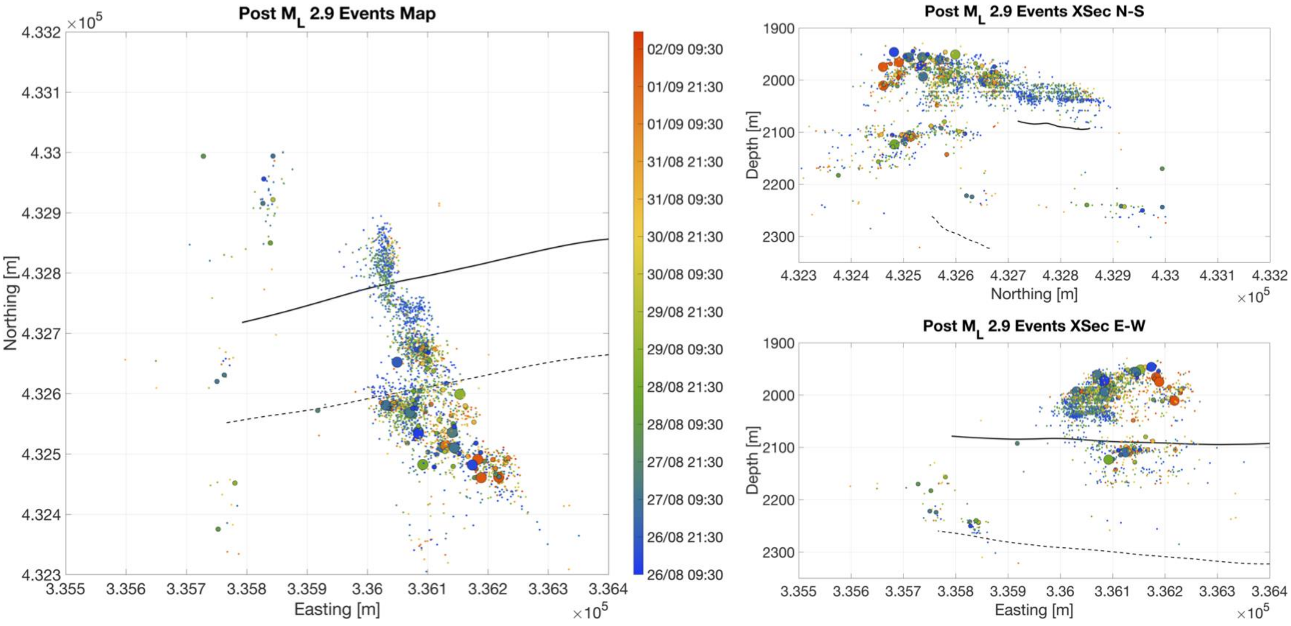

Figure 3.12: Map and cross sections of events that occurred from 1 hour after the M_L 2.9 event until the downhole array was demobilised. Events are coloured by occurrence time and sized by magnitude (see Figure 3.2 for legend).

The NW end of the PNR-2_i fault is found within the SE Zone, in which the largest events occurred. Given the resolution provided by the event location uncertainties, it is possible that all of the larger events occurred on the PNR-2_i fault itself. Alternatively, since faults are often surrounded by smaller fractures with the same orientation, it is possible that some events occurred on such fractures, adjacent to the main fault zone. In either case, our overall interpretation is the same: the southward propagating hydraulic fractures delineated by the Eastern Zone began to impinge on the PNR-2_i fault (and surrounding fractures), producing the larger-magnitude events observed in the SE Zone. Initially, these events are limited to the point of intersection between the hydraulic fractures and the fault. However, the rupture area of the M_L 2.9 event (Figure 3.11) clearly extends beyond and to the SE of this zone. We therefore conclude that this event represented a release of tectonic stresses, where the "runaway rupture" grew along a pre-existing fault, extending beyond the zone that had been perturbed by the injection activity (e.g., Gischig, 2015; Galis et al., 2017). The events that occurred after the M_L 2.9 event are found both within the SE Zone at the intersection of the Eastern Zone hydraulic fracture and the PNR-2_i fault, and along the length of the PNR-2_i fault (Figure 3.12).

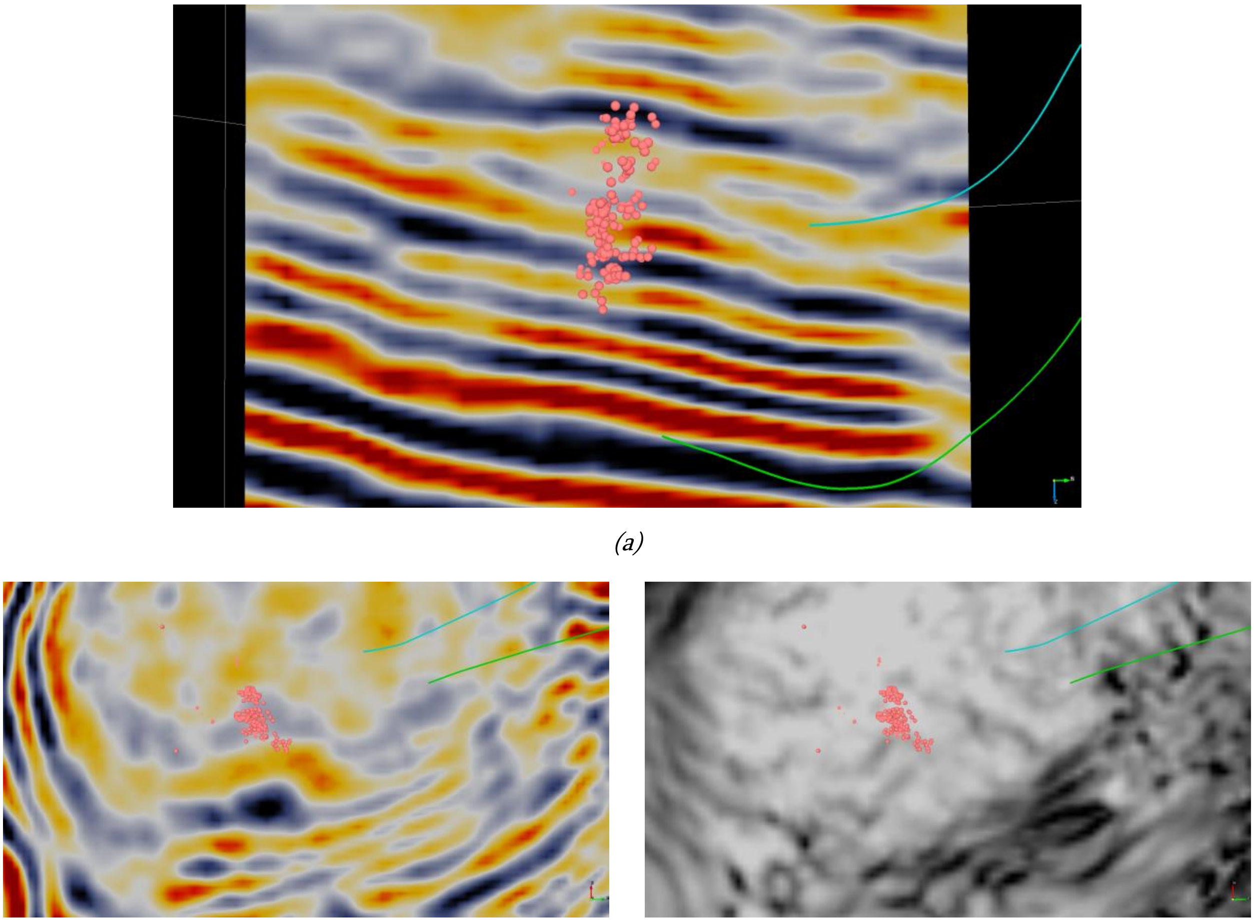

(a)

(b)

(c)

Figure 3.13: Reflection seismic data around the PNR-2 well. In (a) we show a vertical section perpendicular to the PNR-2_i fault (marked by green patch). Note that the vertical axis in this plot is time, creating a vertical exaggeration when compared to the depth. In (b) we show a time-section, and in (c) we show a time-section through a similarity cube. Microseismic events are shown as pink dots.

The NEF-1 fault identified by Clarke et al. (2019) could not be identified within the 3D reflection seismic data acquired at the site. We show 3D reflection data around the PNR-2_i fault in Figure 3.13. There is no obvious manifestation of the fault in vertical sections through this region (Figure 3.13a). This is to be expected because the NEF-1 and PNR-2_i faults produced strike-slip motion. Strike-slip faults are more challenging to identify in vertical sections, since they do not produce vertical offset of beds. In time-sections, the PNR-2_i fault is potentially marked by the offset to the SE of a pair of reflectors (Figure 3.13b), and by the truncation of two zones with low similarity that trend to the NE (Figure 3.13c). However, these features are by no means clear or obvious, so any identification of this fault in the reflection seismic data is ambiguous, at best.

3.3. INTERACTIONS BETWEEN PNR-2 MICROSEISMICITY AND PNR-1Z STRUCTURES

Figure 3.14 shows a map of microseismic event populations from the stimulation of both the PNR-1z and PNR-2 wells. The two wells are separated by approximately 200 m laterally, and 200 m in depth. The three zones of hydraulic fracturing from the PNR-2 well (Western Zone, NS Zone, Eastern Zone) extend above the region stimulated from the PNR-1z well. However, from the cross-section views in Figure 3.14, it is clear that the regions stimulated from the PNR-2 well were shallower, and there is minimal overlap between the two event populations. The PNR-2_ii fault at the northern end of the NS Zone does extend downwards to PNR-1z depths, however it is far to the north of the region stimulated by PNR-1z.

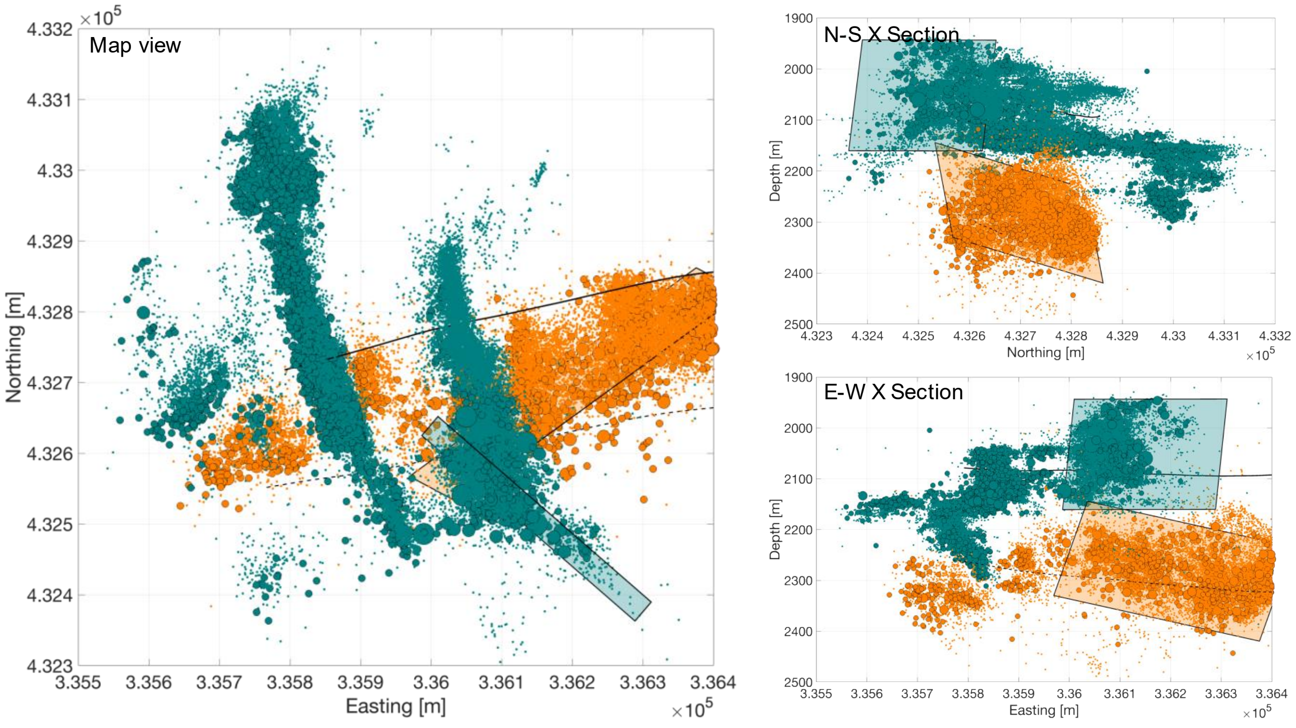

Figure 3.14: Comparison of microseismic event locations during stimulation of the PNR-1z (orange) and PNR-2 (teal) wells. The NEF-1 fault plane identified by Clarke et al. (2019), and the PNR-2_i fault, are shown by the orange and teal planes, respectively. There is minimal overlap between the two event clusters.

The SE zone in which elevated levels of seismicity occurred is located directly above the southwestern end of the NEF-1 fault, which was identified as the causative feature for the PNR-1z seismicity (Clarke et al., 2019a). However, as described above, the SE Zone, and the PNR-2_i fault, are shallower. Moreover, the PNR-2_i fault is clearly delineated by the M_L 2.9 event aftershocks, revealing a fault plane running NW-SE, whereas the NEF-1 fault identified during stimulation of PNR-1z has a NE-SW strike. Therefore, seismicity during stimulation of PNR-2 clearly does not represent activation of the same features that were activated during stimulation of PNR-1z.

It is, however, of interest that the two structures (NEF-1 and PNR-2_i), which have near-orthogonal orientations, are positioned with one directly above the other. One might expect the kinematic interactions between two such features over geological time to produce approaching or intersection damage zones (Peacock et al., 2016), with a higher density of natural fracturing than the surrounding rocks. The increased fracture density could account for the elevated levels of seismicity observed in the SE Zone. However, no such intersection damage zone is required for the interpretation presented above, as this zone of elevated seismicity could simply be associated with a damage zone around the PNR-2_i fault.

4. MAGNITUDE-FREQUENCY DISTRIBUTIONS

The Gutenberg and Richter (1944) b value describes the relationship between the numbers of events and their magnitudes. The cumulative number of events, N, with magnitudes larger than M, is observed to follow a power-law relationship of the form:

$$\log_{10} N = a - bM, \tag{4.1}$$

where a and b are constants to be determined. The a value describes the overall number of events (or the activity), while the b value describes the ratio of large to small events. For example, if $b = 1$, then for 10,000 $M \geq 0$ events, we would expect 1,000 $M \geq 1$ events and 100 $M \geq 2$ events. If $b = 2$ then for 10,000 $M \geq 0$ events we would expect 100 $M \geq 1$ events and 1 $M \geq 2$ event. A large b value therefore implies a larger number of small events relative to large events.

Microseismic event magnitude-frequency distributions can be used to characterise the deformation process that is creating the events (e.g., Verdon et al., 2013). High G-R b values (typically $b \geq 1.5$) imply deformation in an environment with lower stress conditions, where fluid movement is directly driving microseismicity, and where deformation occurs on relatively complex fracture networks. In contrast, low G-R b values (typically $b \approx 1$) represents deformation with high differential stress, where fluids are not playing a direct role, and where slip occurs on simple networks of large, planar features. For example, seismicity associated with hydrothermal fluid and magma movements in volcanoes is often observed to have an elevated b value (e.g., Wyss et al., 1997), whereas seismicity generated by tectonic stresses being released on large faults is observed to have $b = 1$ (e.g., Frohlich and Davis, 1993). These effects are observed to apply across a very wide range of scales, from the laboratory (e.g., Scholz, 1968) to the crustal (e.g., Schlaphorst et al., 2016).

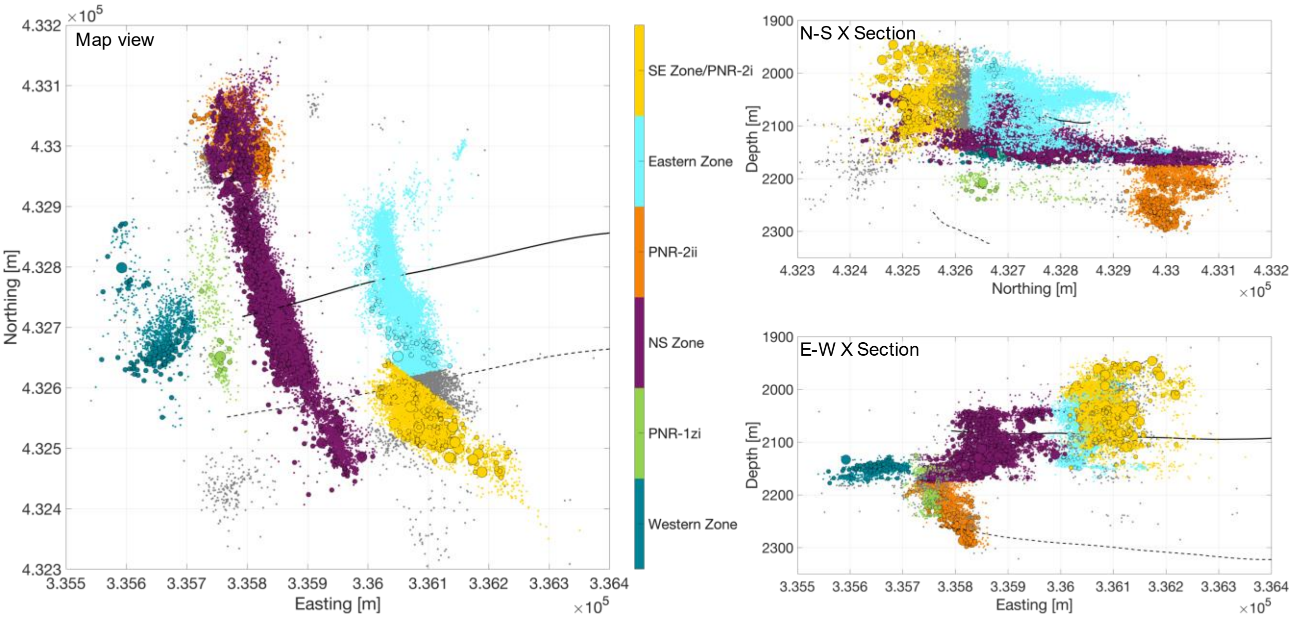

Figure 4.1: Map showing spatial clusters used for G-R b value analysis.

Taking these inferences to the context of hydraulic fracturing, we might therefore assume that high *b* value populations correspond to events directly driven by hydraulic fracture propagation, fluid flow, and pore pressure perturbations, and especially where new fractures are being created. In contrast, low *b* value clusters represent slip that releases tectonic stresses on pre-existing faults. For example, Kettlety et al. (2019) applied these inferences to a hydraulic fracturing dataset from the Horn River Basin, Canada, using *b* value variations to discriminate between events associated with hydraulic fracture propagation and those representing reactivation of pre-existing faults.

In Figure 4.1 we sort the events into clusters representing the key structures described in Chapter 3. We compute the G-R *b* value for each cluster using the Aki (1965) maximum likelihood approach, computing the minimum magnitude of completeness, M_C, using a Kolmogorov-Smirnov test (Clauset et al., 2009) with a 10% acceptance level. The resulting magnitude-frequency distributions, and their corresponding *b* values, are shown in Figure 4.2.

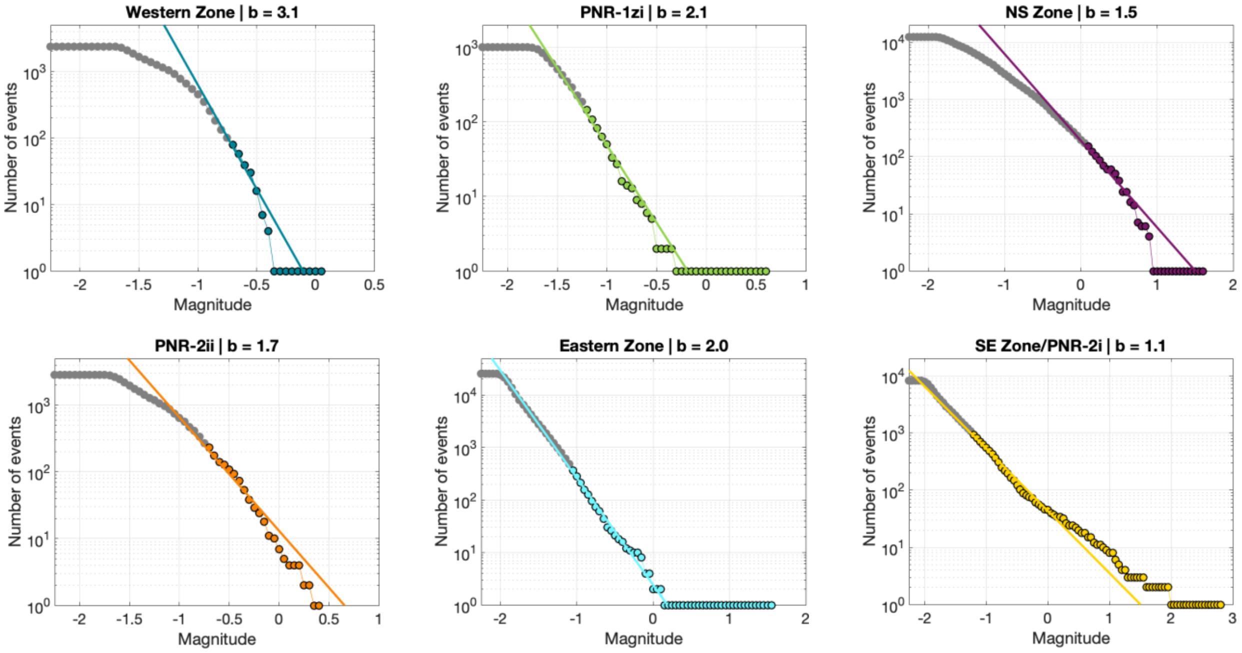

Figure 4.2: Magnitude-frequency plots for each of the clusters shown in Figure 4.1. Dots show observed event populations, solid lines show G-R distributions computed about the minimum magnitude of completeness M_C (shown as the change from grey to coloured dots) computed using a Kolmogorov-Smirnov test.

Our results support the inferences made in Chapter 3. The three zones that we interpreted as representing hydraulic fracture propagation (Eastern, NS, and Western Zones, see Figure 3.2) all have elevated *b* values. The PNR-1z_i and PNR-2_ii structures are also observed to have elevated *b* values. These structures have similar orientations (northward strike, dipping to the east) as some of the seismic discontinuities identified in the 3D seismic data (Cuadrilla Resources, 2019). However, the nature of these structures is not well characterised from any independent geological observations. The observations of high *b* values for these structures in Figure 4.2 leads us to the interpretation that these structures represent zones or corridors of natural fracturing (e.g., Questiaux et al., 2010; Peacock et al., 2016) along which pore pressure pulses are able to propagate, rather than single fault planes on which larger amounts of tectonic stress might be stored.

The SE Zone and the PNR-2_i fault have a magnitude-frequency distribution that is clearly very different to the other clusters. The b value computed in Figure 4.2 is $b = 1.1$, while above $M_W = -0.5$, the observed distribution is actually even flatter, with $b = 0.8$. While all of the other clusters have elevated b values ($b \geq 1.5$), this is the only cluster that has b values that are typical of tectonic faults (e.g., Frohlich and Davis, 1993). As described in Chapter 3, these events correspond to the reactivation of a larger fault on which pre-existing tectonic stresses are released by the seismicity.

5. SPATIO-TEMPORAL EVOLUTION OF MICROSEISMICITY

The evolution of microseismic event distances from the injection point with time can reveal the underlying physical mechanisms that are driving the events (e.g., Shapiro et al., 2006). Shapiro et al. (1997) show that, if microseismicity is driven by pore pressure diffusion from the well, then for constant-rate injection a triggering front should develop that extends in distance, r, from the injection point as a function of time t:

$$r = \sqrt{4\pi Dt}, \tag{5.1}$$

where D is the hydraulic diffusivity. The diffusive case can be contrasted with the case of hydraulic fracture propagation where, assuming minimal leak-off of fracturing fluid, the length of hydraulic fracture propagation might be expected to show a linear time-distance relationship, since the length of a hydraulic fracture L scales with the injection rate Q, the height h_f and width w_f of the hydraulic fracture (Economides and Nolte, 2003; Shapiro et al., 2006):

$$L = \frac{Qt}{2h_f w_f} \quad . \tag{5.2}$$

In Figure 5.1 we show the spatio-temporal evolution of the microseismicity within the western event clusters (Western Zone, PNR-1z_i, NS Zone, PNR-2_ii, see Figure 3.2) for each stage. In Figure 5.2 we show the spatio-temporal evolution of the microseismicity within the eastern clusters (Eastern Zone, SE Zone, see Figure 3.2) for the stages that produced events within this cluster (Stages 4 – 7).

For the PNR-1z microseismicity, we did not observe any clear patterns in r vs t behaviour, with events occurring near-instantaneously at a range of distances from the well (Verdon et al., 2019a). This motivated us to study the effects of stress transfer through the rock frame, since elastic stress transfer through the rock frame occurs at the speed of a compressive wave (1000s of m/s), which is far quicker than any of the timescales considered here.

For the PNR-2 microseismicity, the envelopes of event distances as a function of time appear to evolve with a dependence of $r \propto t^{0.5}$ (curved lines in Figures 5.1 and 5.2). This is indicative of a triggering process driven by pore pressure diffusion. For the western clusters, the events are best approximated by a diffusivity of $D = 2.5$ m^2/s, while the eastern clusters are best approximated by a diffusivity of $D = 1$ m^2/s.

The system permeability, κ can be estimated from the diffusivity by (Shapiro, 2008):

$$\kappa = \frac{D\eta}{n} \quad , \tag{5.3}$$

where

$$n = \frac{h\left(K_d + \frac{4}{3}\mu\right)}{K_d + \frac{4}{3}\mu + \alpha^2 h} \quad ,$$

$$h = \frac{1}{\frac{\phi}{K_f} + \frac{\alpha - \phi}{K_g}} \quad , \tag{5.4}$$

$$\alpha = 1 - \frac{K_d}{K_g} \quad ,$$

where K is the bulk modulus, with subscripts d, g and f corresponding to the dry rock frame, grain material, and fluid; μ is the rock shear modulus; φ is the rock porosity; and η is the fluid viscosity. Using generic values for these properties of $K_d = 20$ GPa, $K_g = 40$ GPa; $K_f = 3$ GPa; $\mu = 10$ GPa; $\varphi = 0.1$; and $\eta = 0.001$ Pa.s, a diffusivity of $D = 2.5$ m^2/s corresponds to a permeability of $\kappa \approx 125$ mD, and a diffusivity of $D = 1$ m^2/s corresponds to a permeability of $\kappa \approx 50$ mD. Note that with generic values, these values should be taken as “order-of-magnitude” estimates, rather than precise values. Estimates for the matrix permeability of the Bowland Shale are typically less than 1 x10^{-4} mD (Clarke et al., 2018), so the values estimated above clearly do not correspond to the matrix permeability of the rock.

Instead, we surmise that the permeabilities estimated from the microseismic event spatio-temporal distributions correspond to the permeabilities of the fracture networks created during hydraulic stimulation. In Chapter 3 we observe that, for most stages, microseismicity occurs along the same zones as reactivated during previous stages (e.g., the NS Zone, and the Eastern Zone). Therefore, the spatial growth of microseismic events will be determined by diffusion of pressure along these features. A permeability of $\kappa \approx 100$ mD is a reasonable value for a stimulated hydraulic fracturing zone (e.g., Liu et al., 2019).

Overall, the consistency of the microseismic event distributions with an $r \propto t^{0.5}$ relationship leads us to conclude that the seismicity is being driven directly by propagation of elevated pore pressures from the well to the fault via the hydraulic fracture networks. This behaviour contrasts with that observed at PNR-1z, where seismicity was driven by stress transfer effects. This serves to highlight that fault reactivation during hydraulic stimulation can occur through a variety of different effects (as described in Chapter 1), and that multiple mechanisms can drive seismicity even at the same site.

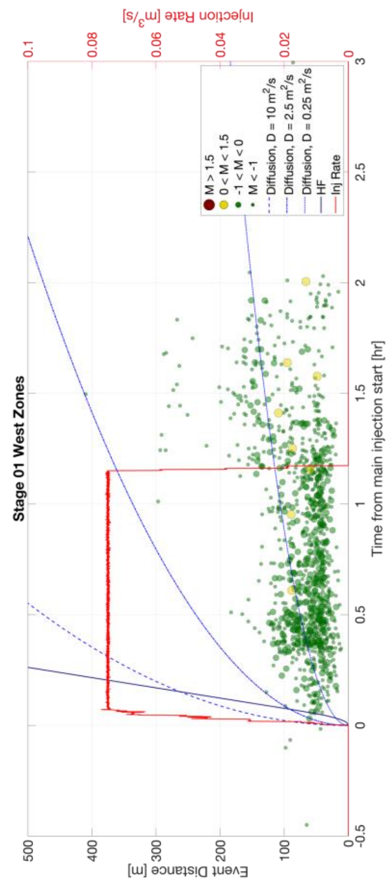
Stage 01 West Zones

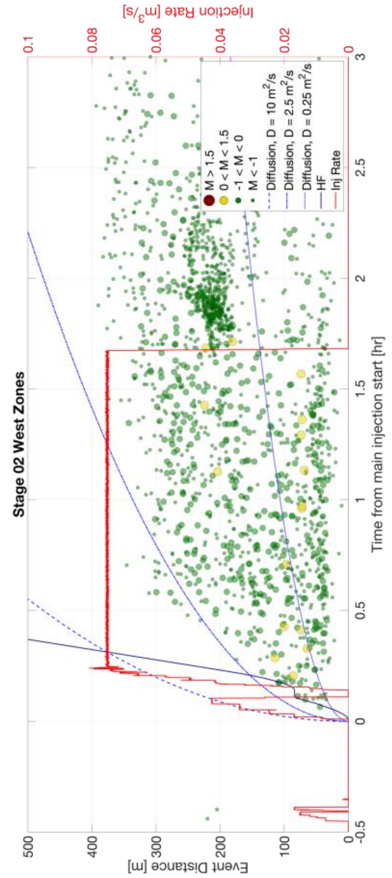
Stage 02 West Zones

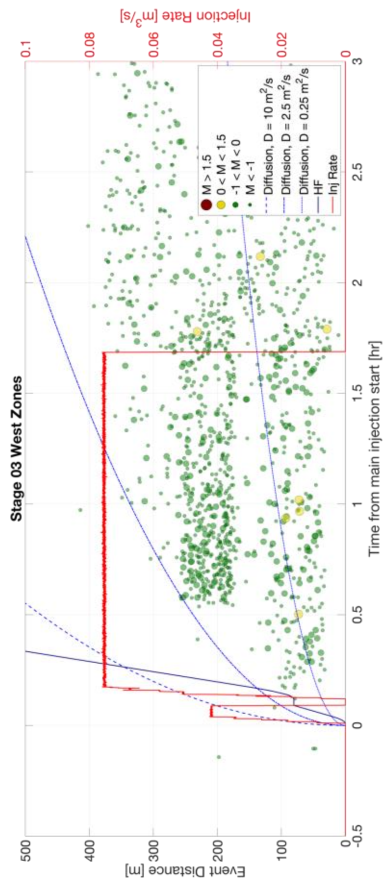
Stage 03 West Zones

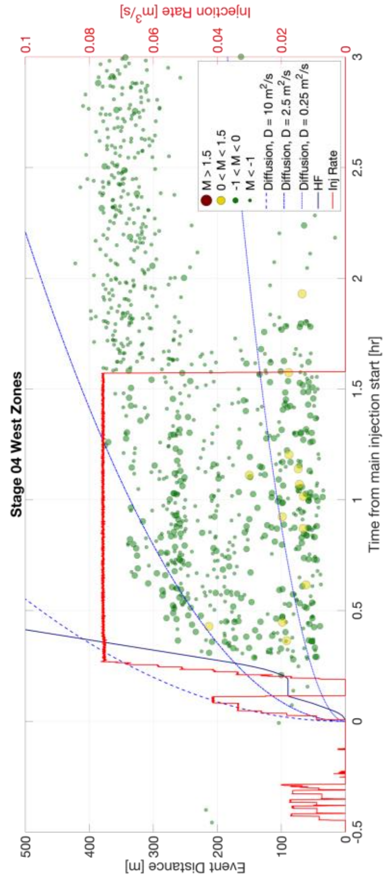
Stage 04 West Zones

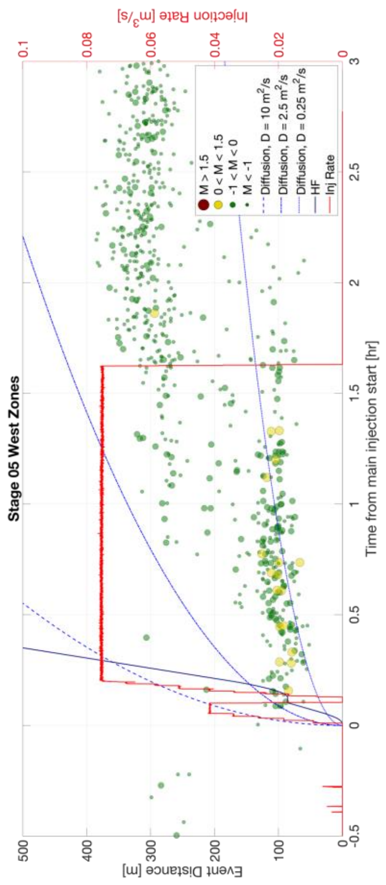
Stage 05 West Zones

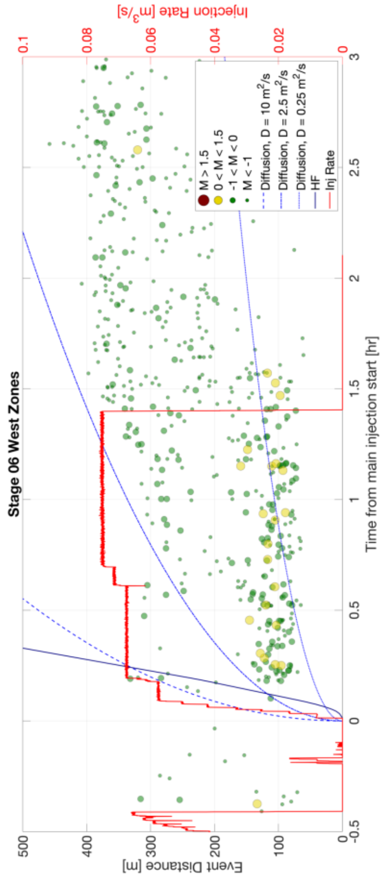
Stage 06 West Zones

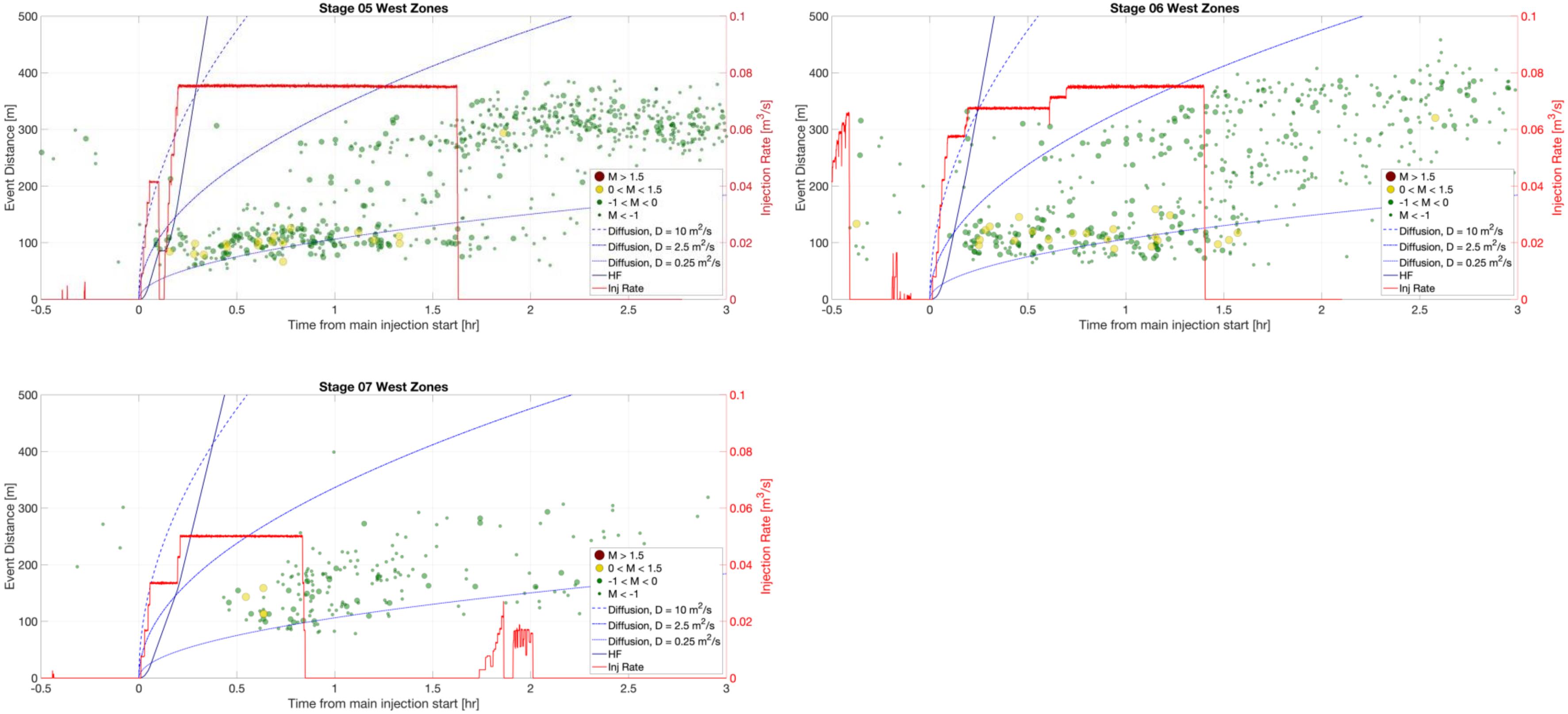

Figure 5.1: Spatio-temporal evolution of microseismicity (dots, coloured and sized by magnitude) within the western clusters for each stage. We also show the injection rate (red line), and the expected time-distance behaviour produced by diffusion models with D = 0.25, 2.5 and 10 m²/s (blue dashed lines), and a hydraulic fracture model assuming h_f = 25 m, w_f = 2.5 mm and no fluid loss (black line).

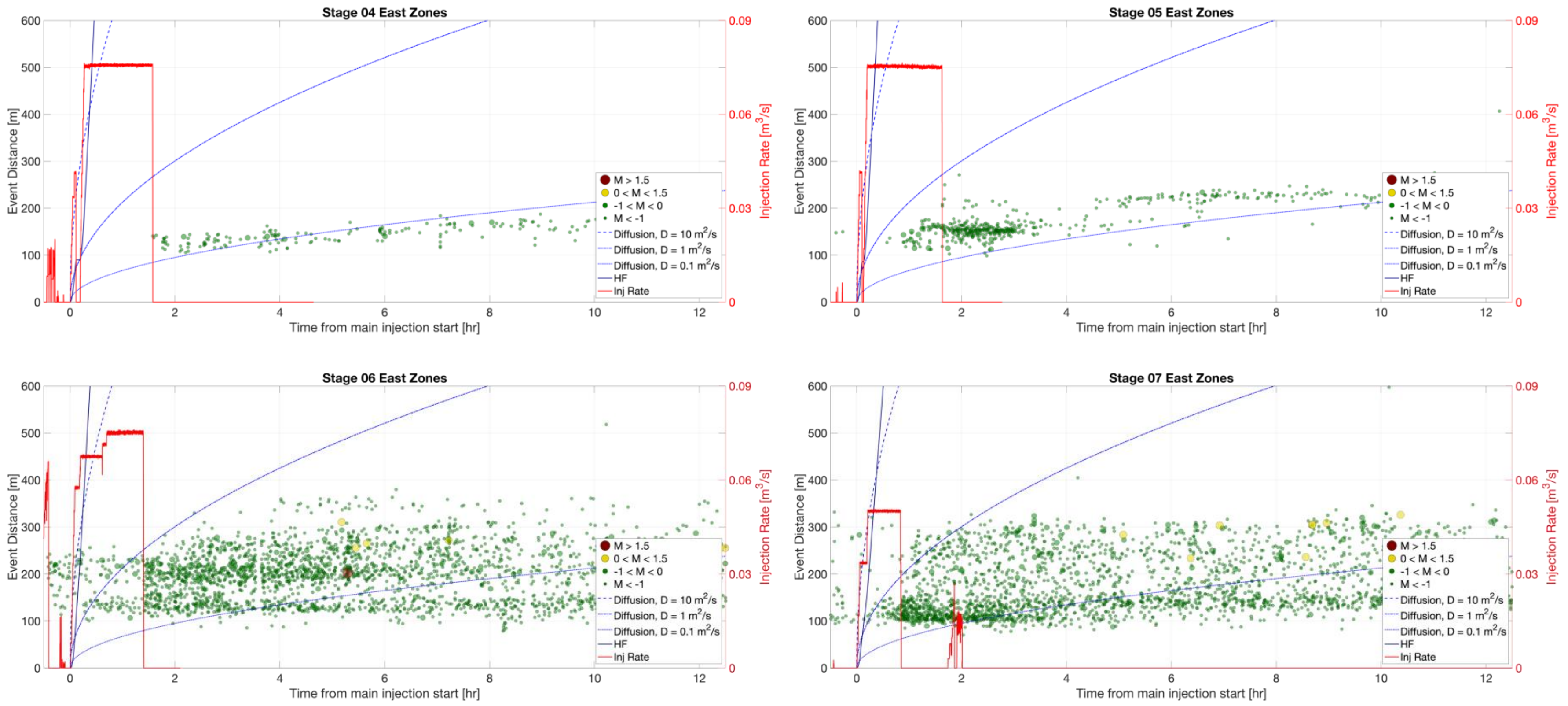

Figure 5.2: Spatio-temporal evolution of microseismicity (dots, coloured and sized by magnitude) within the eastern clusters for Stages 5 – 7. We also show the injection rate (red line), and the expected time-distance behaviour produced by diffusion models with D = 0.1, 1 and 10 m²/s (blue dashed lines), and a hydraulic fracture model assuming h_f = 25 m, w_f = 2.5 mm and no fluid loss (black line).

6. INVESTIGATION OF STRESS TRANSFER EFFECTS

In Chapter 5 we showed that the spatio-temporal evolution of microseismic events is consistent with a process driven by pore fluid pressure diffusion. For the PNR-1z microseismicity we did not observe this behaviour, which motivated us to examine the potential role of static stress transfer from tensile opening of hydraulic fractures as an alternative means of fault reactivation. For PNR-2, while pore pressure diffusion effects appear to dominate the evolution of microseismicity, it is still of interest to assess whether the tensile opening of hydraulic fractures could also have promoted slip on the fault.

6.1. STATIC STRESS MODELLING METHOD

We examine stress transfer effects using the analytical solutions for tensile fracture opening developed by Okada (1992), using the PSCMP code developed by Wang et al. (2006). We computed changes in Coulomb failure stress, ΔCFS (Equation 1.2), where a positive ΔCFS implies that a fault is being moved towards the failure envelope, increasing the likelihood of induced seismicity.

For the PNR-1z microseismicity (Verdon et al., 2019a), the positions and orientations of the hydraulic fractures during each stage were not well constrained, since there was considerable overlap between the loci of the hydraulic fracturing and the reactivated structures. While we defined the NEF-1 fault plane based on microseismic observations, we maintained an ambivalence as to whether this feature was a single fault plane or a zone of fracturing. We therefore assessed the role of stress transfer by computing the Coulomb Index, which describes the proportion of microseismic events located in regions where ΔCFS is positive. We found that a large proportion of events did occur in positive ΔCFS areas, indicating that static stress transfer from tensile hydraulic fracture opening was playing a significant role in the microseismicity (Verdon et al., 2019a; Kettlety et al., 2020).

For the PNR-2 seismicity, the growth of the hydraulic fractures is much more clearly defined by the observed events (the NS Zone and the Eastern Zone described in Chapter 3). Similarly, the fault plane responsible for the M_L 2.9 event is clearly delineated by its aftershocks (Figure 3.11). As such, rather than computing ΔCFS values for the microseismic events, a more instructive approach is to compute the ΔCFS values on the PNR-2_i fault itself.

As the input, or loading, for our stress transfer simulations, we followed our previous approach (Verdon et al., 2019a), using a stochastic representation of the expected hydraulic fracture distribution. For PNR-2 we defined two source zones based on the observed microseismic clusters – the main NS Zone, and the Eastern Zone. For each, we assigned statistical distributions to parameterise the hydraulic fractures, from which the source populations were drawn. We performed 1,000 model instances for each source zone, and in the following sections used the median stress changes to assess the impact of these fractures on the surrounding rock mass.

These statistical distributions are as follows for the NS Zone:

- Fracture initiation points are normally distributed around the mid-point of Sleeve 1, with standard deviations of 15 m along the well, and 10 m perpendicular to the well (vertically and laterally).
- Two thirds of fractures propagate to the north, and one third propagate to the south.
- The northward-propagating fractures have a strike of 350°, while the southward propagating fractures have a strike of 155°.
- The northward-propagating fractures are drawn from a uniform length distribution with a maximum of 375 m. The southward propagating fractures are drawn from a uniform length distribution with a maximum of 300 m.
- The tensile opening of all fractures is taken as 2 mm. The aspect ratio of the fractures is such that the fracture height/width is 0.2.

For the Eastern Zone:

- Fracture initiation points are normally distributed around the mid-point of Sleeve 13, with standard deviations of 10 m in all directions.
- Four fifths of fractures propagate to the north, and one fifth propagate to the south.
- The northward-propagating fractures have a strike of 345°, while the southward propagating fractures have a strike of 165°.
- The northward-propagating fractures are drawn from a uniform length distribution with a maximum of 100 m. The southward propagating fractures are drawn from a uniform length distribution with a maximum of 200 m.
- The tensile opening of all fractures is taken as 2 mm. The aspect ratio of the fractures is such that the fracture height/width is 0.2.

For both source zones, we populated fractures from these distributions until the volume of the hydraulic fractures meets the total injection volume for the zone, as determined from the injected volumes. This requires an estimate of the relative proportions of each stage volume that might have contributed to each fracture zone. This can’t be easily quantified with the available data. We therefore made the arbitrary assumptions shown in Table 6.1, based on the relative proportions of microseismic observed on each feature during each stage. In addition, we assumed an arbitrary 50% leak-off factor. Examples of the resulting model sources are shown in Figure 6.1. We modelled all of the sources as producing strain perpendicular to the fracture face (tensional, mode 1 slip), with no component of slip parallel to the fracture face.

Stage	Volume [m³]	% into NS Zone	% into Eastern Zone
1	323	100	0
2	419	100	0
3	432	100	0
4	347	90	10
5	308	75	25
6	259	60	40
7	64	40	60
Total Vol (assuming 50% leak-off) [m³]:		1076	205

Table 6.1: Injection volumes for each stage, and our apportionment of their volumes into the NS and Eastern hydraulic fracturing zones.

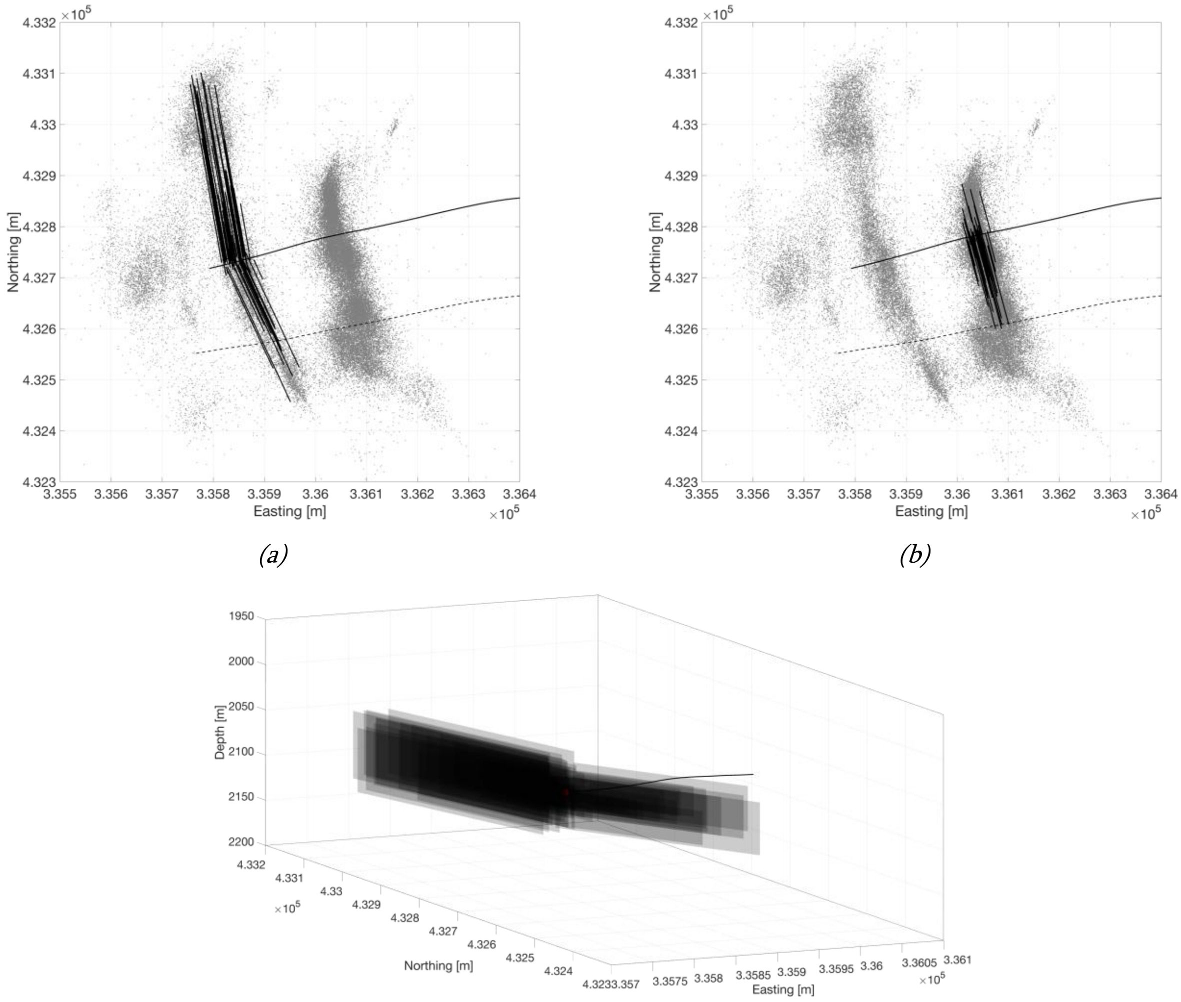

(a) *(b)*

(c)

Figure 6.1: Tensile hydraulic fracture 'sources' used to simulate stress changes in the surrounding rocks. In (a) we show a map view of the sources for the NS Zone (black lines) with the observed microseismicity overlain (grey dots), in (b) we show the same for the Eastern Zone. In (c) we show a 3D view of the NS Zone sources.

We used the PSCMP code (Wang et al., 2006) to compute the stress changes produced by these sources, resolving these onto the PNR-2_i fault plane, with a strike of 140°, dip of 85°, and a rake of 180°, to compute ΔCFS. We assume a friction coefficient of $m = 0.6$, and Lamé parameters for the rock of $\mu = \lambda =$ 25 GPa.

We note that the amount of fractures, and therefore the magnitude of any stress change, will be determined by the number of fractures, and therefore the assumed volumes (Table 6.1), whereas the style of the deformation, i.e. whether a region experiences a positive or negative ΔCFS, will be determined by geometry and orientation of the fractures with respect to the fault. Therefore, in the following results, the magnitude of the stress changes may be relatively poorly constrained. However, since the geometry of the hydraulic fractures is relatively well constrained by the microseismicity, the sign of the ΔCFS change (i.e. positive or negative) will be relatively robust. The focus of our interpretation is on the sign of the ΔCFS value, since this determines whether deformation is pushing faults toward or away from failure.

6.2. RESULTS

Figure 6.2 shows maps of ΔCFS changes at the well depth produced by both the NS Zone and Eastern Zone sources. In both cases, ΔCFS values decrease in the regions either side of the fractures, and increase in zones ahead of the fracture tips. In Figure 6.3 we show the ΔCFS values across the PNR-2_i fault plane. We find that the lowermost corner of the fault nearest to the fracture zones experiences negative ΔCFS changes. However, most of the PNR-2_i fault plane, including the region defined as the rupture area by the M_L 2.9 event aftershocks (see Chapter 3) experiences positive ΔCFS changes from the tensile opening of fractures in both the NS and Eastern zones. These observations indicate that static stress transfer may again be playing a role in facilitating slip on a pre-existing fault, as was the case for the PNR-1z stimulation.

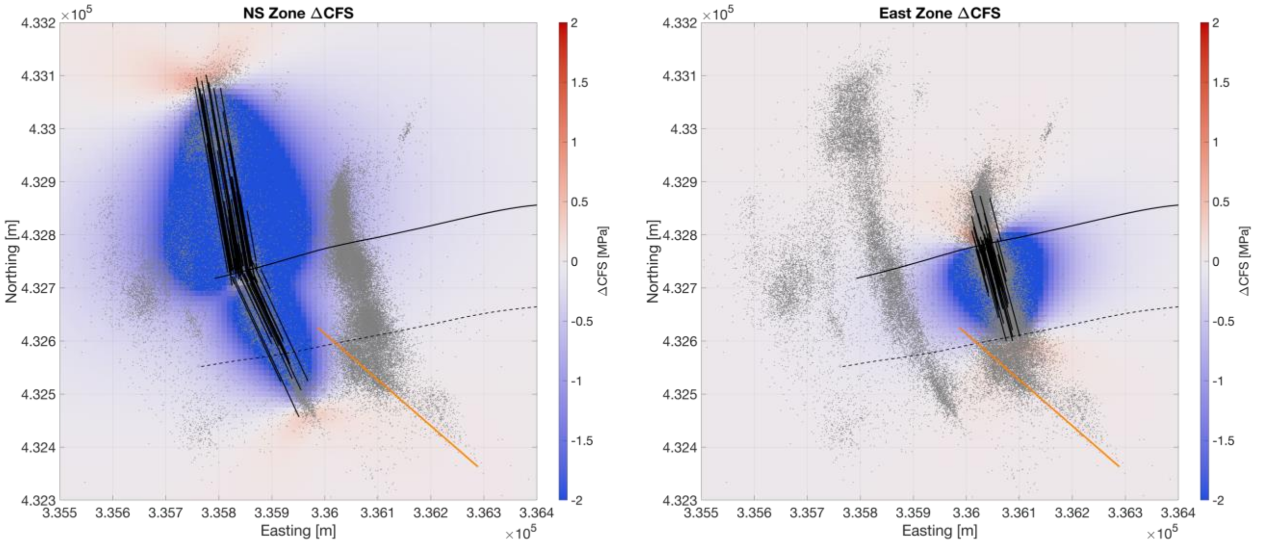

(a) *(b)*

Figure 6.2: Maps of ΔCFS produced by the NS Zone (a) and the Eastern Zone (b). In each case a representation of the sources is shown by black lines, the observed microseismicity by grey dots, and the PNR-2_i fault by the orange line.

However, as described in Chapter 5, the spatio-temporal evolution of the microseismicity shows a clear relationship between time and distance that is indicative of a diffusion-driven process. If static stress transfer were the dominant process, then we would expect a near-instantaneous response with events occurring at a range of distances with little dependence on time. Therefore, while these stress transfer effects may be acting to promote slip on the PNR-2_i fault, overall the microseismicity is driven by the diffusion of elevated pore pressures from the well. Nevertheless, these results show that establishing the causative processes for induced seismicity can be challenging, and that multiple physical processes can act in tandem to reactivate faults during hydraulic stimulation.

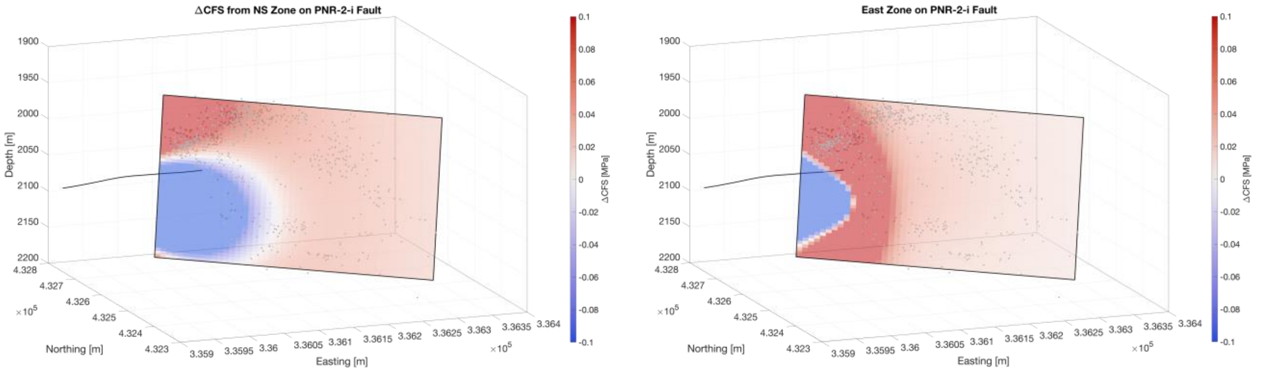

(a) *(b)*

Figure 6.3: ΔCFS values on the PNR-2_i fault plane (as defined by the M_L 2.9 event aftershocks, shown as grey dots) produced by the NS Zone (a) and the Eastern Zone (b).

6.3. UNDERSTANDING THE EASTERN ZONE OF HYDRAULIC FRACTURING

In Chapter 3 we detailed how, from Stage 4 onwards, we began to see the creation of the new zone of hydraulic fracture propagation to the east of the active injection stages (the Eastern Zone in Figure 3.2). This zone initiated at approximately the position of Sleeve 13, roughly 100 m east of the Stage 4 injection point. It is this zone which ultimately provided the connection for the elevated pore pressure perturbations to reach the PNR-2_i fault. Similarly, we saw microseismic events that indicated hydraulic fracture propagation to the west of the well toe (the Western Zone in Figure 3.2), which is also over 100 m westward of the injection point (although this zone was less significant from the perspective of fault reactivation, since it did not connect to any seismogenic features).

In this section we therefore address potential mechanisms for the creation of these zones, with a focus on the Eastern Zone since this is ultimately responsible for the induced seismicity. While doing so, we note that a robust answer to this question is not necessary to explain the occurrence of induced seismicity during stimulation of PNR-2. Had this zone of fractures not initiated and grown in this position during stimulation of Stages 4 – 7, it seems inevitable that similar fractures would have been created during stimulation of later stages (e.g., Stages 10 – 15), resulting in the same eventual impacts on the PNR-2_i fault. However, the creation of the Eastern Zone over 100 m to the east of the active stages meant that the fault was intersected earlier than it might otherwise have been.

The effects of stress shadowing (e.g., Nagel and Sanchez-Nagel, 2011; Dohmen et al., 2014) may have played a significant role. The tensile opening of hydraulic fractures in the direction of the minimum stress, which at the PNR site is horizontal and striking at 83° (Clarke et al., 2019b), produces an increase in compressive stress in the surrounding rock mass.

The formation breakdown pressure, P_b, at which hydraulic fractures will begin to propagate, can be estimated as (Haimson and Fairhurst, 1967):

$$P_b = 3\sigma_h + \sigma_H - P + T_0 \quad , \qquad (6.1)$$

where σ_h and σ_H are the minimum and maximum horizontal stresses, and T_0 is the tensile strength of the rock. As such, P_b, and thereby the ability of hydraulic fractures to form, is primarily dependent on changes to the minimum stress. If tensile opening of nearby fractures increases the minimum horizontal stress, then it will suppress hydraulic fracture formation in the surrounding rock mass.

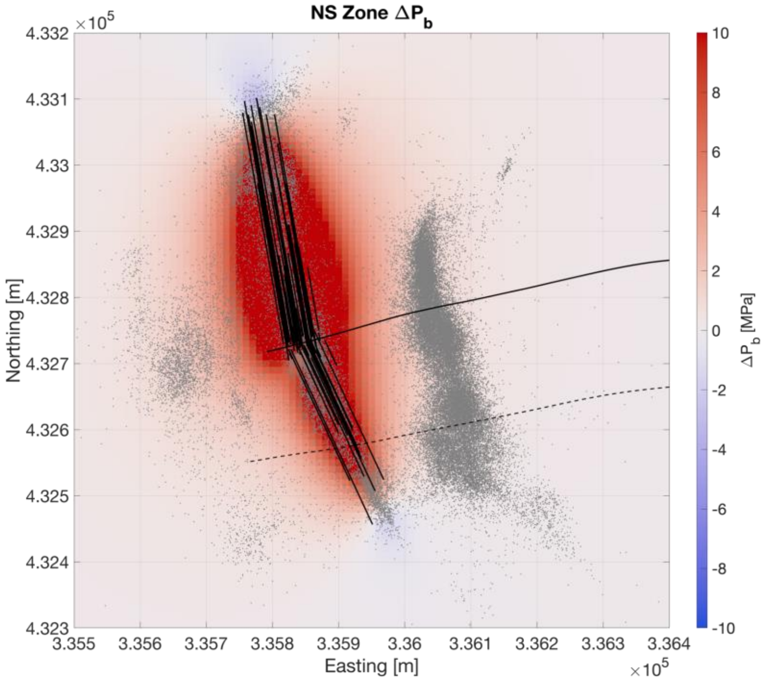

Figure 6.4: Map showing changes formation breakdown pressure, P_b, estimated from modelled changes in maximum and minimum stresses produced by the tensile opening of fractures in the NS Zone. The increase in breakdown pressure may inhibit hydraulic fracture nucleation in the immediate vicinity of the NS zone, favouring fracture opening further along the well to both the east and west.

To investigate this effect, we computed stress changes created by the tensile opening of fractures in the main NS source zone using the methods described in Section 6.1. We used the modelled changes in σ_h and σ_H to compute changes in P_b (or ΔP_b), shown in Figure 6.4. We observed a significant increase in P_b of $\Delta P_b > 5$ MPa within approximately 100 m of the NS Zone. Both the Western and Eastern zones of hydraulic fracturing are found in regions where the ΔP_b increase is less than 3 MPa. This suggests that stress shadowing may indeed have played an important role in controlling where subsequent zones of hydraulic fracturing were able to form after the initial NS Zone had formed.

We also examined whether any pre-existing structures could have influenced the nucleation of the Eastern Zone. Figure 6.5 shows a cross-section through the 3D reflection seismic data cube running parallel to the PNR-2 well, with the microseismicity overlain. We note the presence of a gentle anticline running roughly north-south, with the hinge located in approximately the same position as the nucleation point of the Eastern Zone. Typically, one might expect a higher intensity of natural fracturing at the anticline hinge (Figure 6.6), with the fractures running along the hinge direction (e.g., Gholipour et al., 2016), which in this case would be north-south. The reflection amplitudes increase slightly at the crest of this anticline, which could also indicate a change in aggregate rock properties, potentially created by a change in fracture intensity (a full inversion of the 3D data for variations in rock physics properties is beyond the scope of this study). The presence of increased natural fracturing with an orientation close to that of θ_{SHMAX} would promote the occurrence of hydraulic fracturing along this same axis at this position.

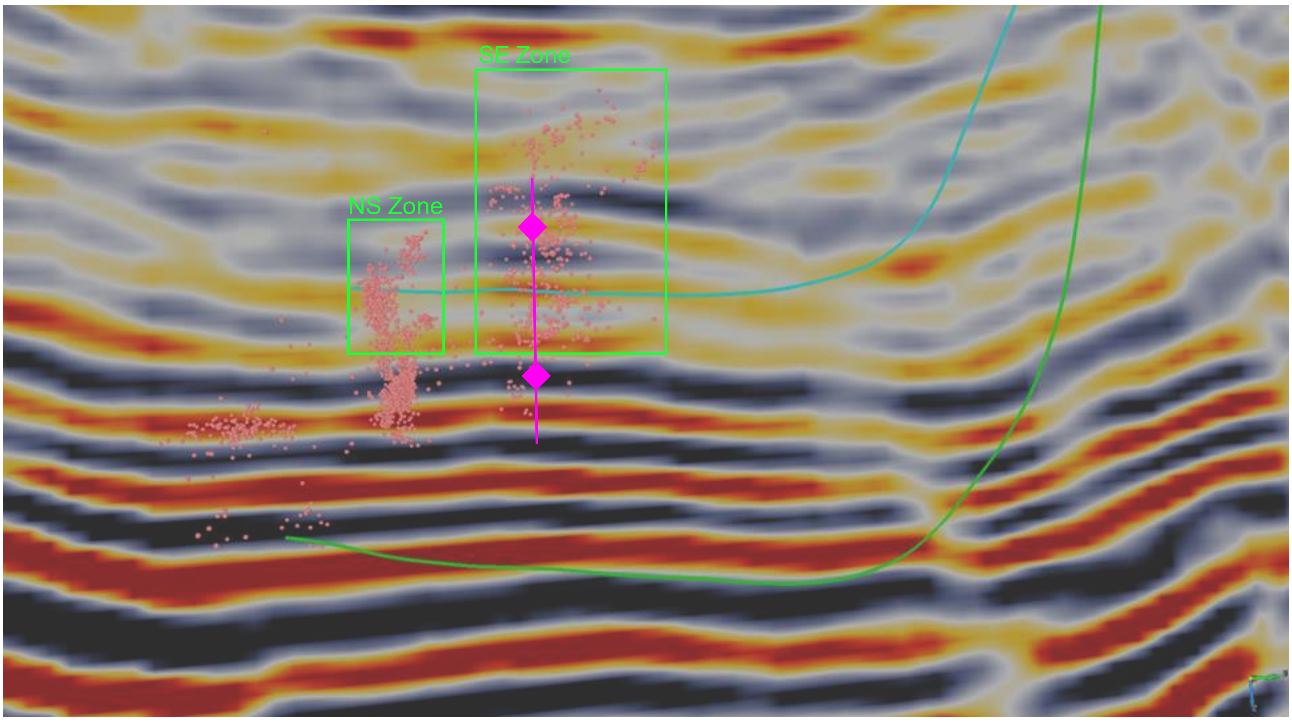

Figure 6.5: Vertical section through the reflection seismic survey cube, running parallel to the PNR-2 well (cyan), with the PNR-1z well also shown (green line). Events with $M_W > -1.0$ are marked by pink dots. Note that the vertical axis in this plot is time, creating a vertical exaggeration when compared to the depth sections shown in Section 3. A gentle anticline with a N-S axis, is found at the position where the Eastern Zone develops from the PNR-2 well (magenta). Seismic amplitudes also increase at this point.

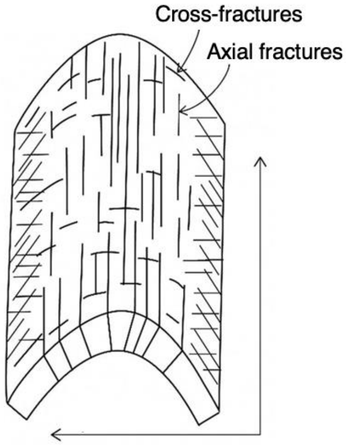

Figure 6.6: Schematic depiction of fractures around an antiform: we might expect a higher intensity of fractures around the hinge, with fracture strikes matching the fold axis. Image adapted from Gholipour et al. (2016).

While these structural factors might account for the position of the Eastern Zone, the Western Zone of hydraulic fracturing is not situated on such a feature. Therefore, our preferred explanation for the separation of the Eastern and Western Zones from the main NS Zone, despite injection in close proximity to the main zone, is the stress shadowing effect described above. However, the presence of natural fractures along the crest of the gentle anticline shown in Figure 6.5 could also have facilitated the formation of the Eastern Zone.

The vertical stress gradient at the PNR site is estimated to be 0.026 MPa/m and the minimum horizontal stress gradient is 0.017 MPa/m (Clarke et al., 2019b), giving stress values at the depth of the PNR-2 well (~2,100 m) of 54.6 MPa and 35.7 MPa, respectively. Figure 6.7 shows the modelled bottom-hole pressure for each of the injection stages. We note that injection in Stages 4 – 7, when microseismicity was observed along the Eastern Zone, took place at pressures that were larger than the vertical stress. This raises the possibility that the injection was able to create tensile opening of bedding planes (e.g., Huang and Liu, 2017), which provided the pathway by which elevated fluid pressures were transferred from the injection sleeves to the Eastern Zone, at which point, being beyond the influence of the stress shadow created by the tensile fractures in the NS Zone, further hydraulic fracturing was able to occur.

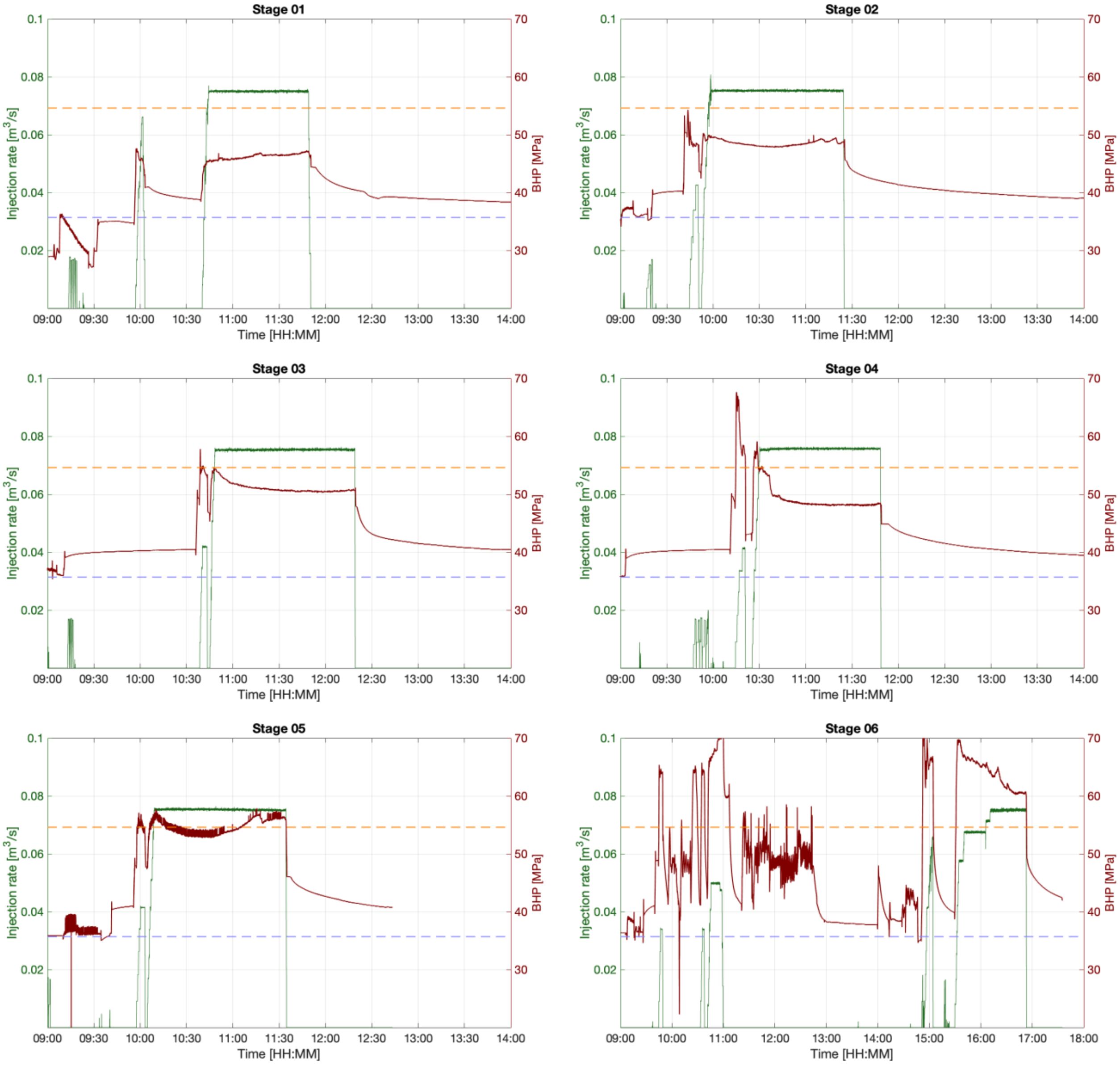

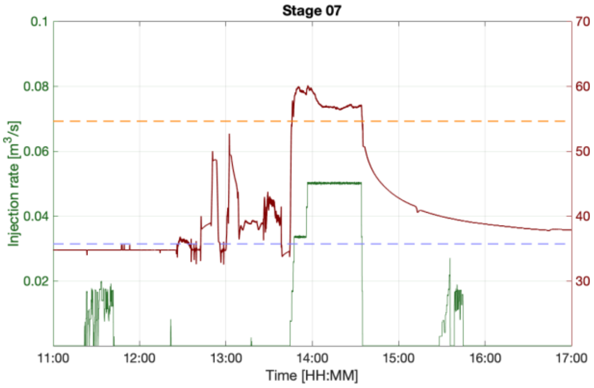

Figure 6.7: Injection rates (green) and modelled bottom-hole pressures (red) for each injection stage. We also show the estimated minimum horizontal (blue) and vertical (orange) stress conditions from Clarke et al. (2019b). Injection pressure for the latter stages exceed the vertical stress, raising the possibility of bedding-plane opening.

7. ORIENTATION OF FAULTS WITHIN THE IN SITU STRESS FIELD

The two faults that were reactivated at the PNR site produced markedly different levels of seismicity. The largest event on the NEF-1 fault, reactivated during stimulation of the PNR-1z well, had a magnitude of M_L 1.5. The PNR-2_i fault produced a magnitude M_L 2.9 event. This represents a difference in seismic moment of over 100 times. The oblique orientation of the NEF-1 fault with respect to the well meant that it was intersected by many hydraulic fracturing stages, whereas the PNR-2_i fault received injection from, at most, 3 stages. We estimate that the stages that intersected the PNR-1z NEF-1 fault injected over 2,000 m^3 of fluid, whereas the combined injection volume of Stages 5, 6 and 7 in PNR-2 was approximately 1,000 m^3.

Numerous studies have observed that the seismicity rate and cumulative moment release scales with the injection volume (e.g., Shapiro et al., 2010; Hallo et al., 2014; Verdon and Budge, 2018; Clarke et al., 2019a; Kwiatek et al., 2019). However, in this case the smaller volume at PNR-2 produced a larger seismic response. The rate of seismicity as a function of volume can be characterised by the seismogenic index (Shapiro et al., 2010). Clarke et al. (2019a) found that the seismogenic index during reactivation of the NEF-1 fault was $SI \approx -1.8$. In contrast, the seismogenic index for the PNR-2_i fault is $SI > -1$, representing an order of magnitude more events per unit of fluid volume injected. It is therefore of interest to investigate potential reasons for the difference between the responses of the two faults.

One consideration is fault size, since earthquake magnitude is limited by the dimensions of the fault on which rupture can occur (Equation 3.1). However, the NEF-1 fault is approximately 500 m long, and 200 m high, giving an area of 100,000 m^2, whereas the PNR-2_i fault, as documented in Chapter 3, has an area of approximately 65,000 m^2. Therefore, based on their respective areas, we would again anticipate that the NEF-1 fault might be able to host larger events. Of course, this argument cannot account for the fact that, as discussed by Verdon et al. (2019a), the NEF-1 "fault" may in fact represent a zone of fracturing, with no single plane on which larger events could occur.

An alternative consideration is the orientations of the NEF-1 and PNR-2_i faults within the *in situ* stress field. From Equation 1.2, the higher the *CFS* acting on a fault, the smaller the perturbation required to exceed the Coulomb failure envelope. Hence, we might expect a fault with lower *CFS* to reactivate more quickly, and produce larger events for a given injection volume.

For two faults within the same stress field, their *CFS* values will be determined by their respective orientations. We investigate these effects using the stress field determined by Clarke et al. (2019b) for the PNR site, listed in Table 7.1. We use these values to calculate the critical pore pressure increase, P_C, required to exceed the Coulomb failure threshold:

$$P_C = \sigma_n - |\tau|/m. \tag{7.1}$$

In this formulation, a low P_C value indicates that a small perturbation is sufficient to allow slip to occur on a fault, while a high P_C value indicates that a fault is relatively stable, and a large perturbation is required for slip to occur (e.g., Walsh and Zoback, 2016; Kettlety et al., 2019).

The resulting values for P_C at the depths of the PNR-1z and PNR-2 wells are shown in Figure 7.1, using a generic value of $m = 0.6$. We find that the PNR-1z NEF-1 fault is moderately well orientated in the stress field, with a P_C value of 11 MPa. The orientation of the NEF-1 fault is derived from fitting a plane to a combined population of the larger events during PNR-1z stimulation, and the events that occurred during the injection hiatus in PNR-1z (Clarke et al., 2019). We estimate uncertainties for the estimated orientation of the NEF-1 fault of ±15° in strike, and ±10° in dip. Within this range of values, P_C may vary between $-1 < P_C < 24$, and this does not account for any uncertainties in stress gradients or orientation.

	Gradient [MPa/m]	Uncertainty
σ_{HMAX}	0.032	0.006
σ_{hmin}	0.017	0.004
σ_V	0.026	0.001
P	0.012	0.001
θ_{SHMAX}	173°	7

Table 7.1: 1D geomechanical model for the PNR site, giving stress gradients, σ_{HMAX} orientation, and their uncertainties.

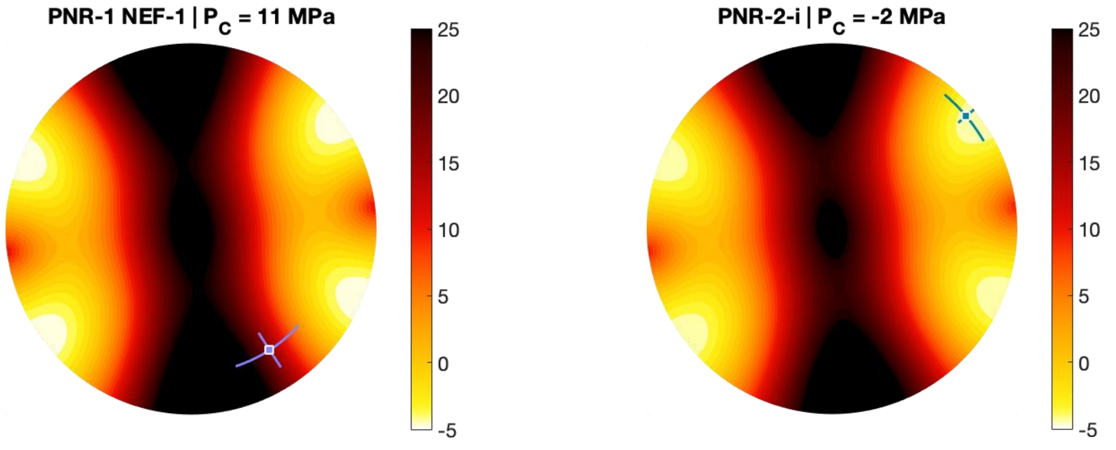

(a) *(b)*

Figure 7.1: Critical pore pressure, P_C, as a function of fault orientation for the PNR-1z (a) and PNR-2 (b) depths. Position on the stereographic projection represents the fault-normal orientation. The coloured squares show the orientations of the NEF-1 and PNR-2_i faults, and their uncertainties (coloured lines), with the P_C values for each listed in the figure titles.

Walsh and Zoback (2016) developed a Monte Carlo approach to incorporate uncertainties in both fault orientation, friction coefficient, and stress state, into a Quantitative Risk Assessment (QRA) for the fault slip potential. We use 100,00 random instances of the stress state, fault orientation, and friction coefficient, drawing values from the uncertainties for the σ_{HMAX}, σ_{hmin}, σ_V, and pore pressure gradients listed in Table 7.1, with $m = 0.6 \pm 0.1$. The uncertainty in orientation for NEF-1 is listed above, while the PNR-2_i fault is better-constrained by the M_L 2.9 event aftershocks, so we assign uncertainties of ±10° in strike, and ±5° in dip.

We display the results as a cumulative distribution function, showing the likelihood that the Coulomb failure threshold is exceeded for a given pore pressure perturbation (Figure 7.2). This plot shows that, given the uncertainties in fault orientation and stress state, there is a wide range of possible P_C values for both faults. However, the PNR-2_i is clearly far closer to the Coulomb failure threshold in the *in situ* stress field. Approximately 85% of the scenarios for the NEF-1 fault have $P_C > 0$, and more than 50 % of scenarios have a $P_C > 15$ MPa, implying that a significant pore pressure perturbation is required for fault reactivation. In contrast, for the PNR-2_i fault, more than 50 % of scenarios have $P_C < 0$ MPa, implying that the fault is at the point of criticality, and therefore able to slip with minimal perturbation.

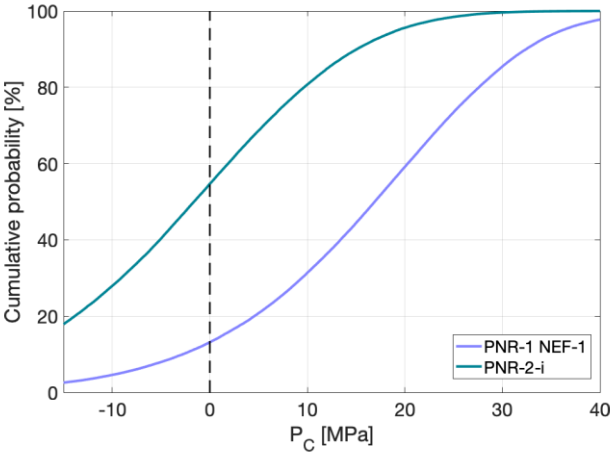

Figure 7.2: Cumulative probability curves showing P_C for the NEF-1 (blue) and PNR-2_i (teal) faults.

These observations provide a compelling explanation for the significant difference in the levels of seismic response between the PNR-1z NEF-1 and PNR-2_i faults. The PNR-1z fault is moderately well aligned in the *in situ* stress field, but a large perturbation is required to exceed the Coulomb failure threshold. As such, the fault is relatively slow to reactivate, with seismicity building up slowly as it was intersected by multiple injection stages. While this may simply be a factor of the fault's position, there was minimal reactivation of the NEF-1 fault outside of the stimulated zone.

In contrast, the PNR-2_i fault is very well aligned in the *in situ* stress field, with relatively minor perturbations being sufficient to induce failure. As such, once it was reached by the fractures extending from the Eastern Zone, it was relatively quick to reactivate, producing large events relative to the small volumes that reached it via this pathway. Moreover, as the aftershocks show, the rupture area of the M_L 2.9 event extended a substantial distance, roughly 200 m, away to the SE from the region where it was intersected by the Eastern Zone hydraulic fractures. Evidently, this represents a "runaway rupture" (e.g., Gischig, 2015; Galis et al., 2017) in the sense that the rupture extends beyond the zone that has been perturbed by the injection activity, releasing stored tectonic stress along the fault. This phenomenon is favoured in situations where the stress conditions along the fault are close to failure prior to perturbation (Gischig, 2015), as is the case for the PNR-2_i fault.

These observations show the importance of the pre-existing stress conditions, and the orientations of faults within them, in determining the seismic response that they will produce to injection. We anticipate that faults which are close to the Coulomb failure threshold will produce more seismicity for a given injection volume.

8. CONCLUSIONS

In this study we examine and interpret the microseismicity recorded by a downhole geophone array during hydraulic fracturing of the PNR-2 well at the Preston New Road site, Lancashire. Our focus is on understanding the causative mechanisms by which the hydraulic fracturing produced earthquakes of sufficient size to be felt by the public nearby.

The spatial and temporal evolution of the microseismicity, combined with their G-R b values, reveals the growth of hydraulic fractures from the well, extending along the direction of maximum horizontal stress (NNW-SSE). The first 4 stages appear to have injected fluid into the same growing hydraulic fracture zone. These stages also produced a second zone of hydraulic fracturing to the west of the well toe, and interacted with two zones of fracturing that extended below the stimulated zone. Neither of these features produced seismicity of any significant magnitude. From the latter part of Stage 4 and onward, a new zone of hydraulic fracturing initiated further east along the well, roughly at the position of Sleeve 13. The zone propagated to the south, and ultimately began to cause elevated levels of seismicity on the PNR-2_i fault. Magnitude $M_L > 0.5$ events occurred after Stage 6, entailing a pause in injection. The operator injected a reduced volume for Stage 7. No $M_L > 0$ events occurred during injection. However, seismicity began to escalate in the hours after injection, ultimately culminating in the occurrence of the M_L 2.9 event, which occurred over 60 hours after the cessation of injection.

The aftershocks from the M_L 2.9 event clearly delineate its rupture, with the area of rupture matching that expected from the moment release. The fault responsible extends to the SE from the southern tip of the later, eastern zone of hydraulic fracturing. The rupture area extends beyond the part of it that was directly intersected by the hydraulic fracturing, indicating a “runaway” rupture beyond the stimulated area, releasing tectonic stress along a fault. There is no clear evidence for this fault in the 3D reflection seismic data, highlighting once again the challenges of detecting small faults in this way, particularly if they have a strike-slip sense of displacement.

There is little or no overlap between the PNR-2 microseismicity and that recorded during stimulation of PNR-1z. Evidently, the separation between the wells, of c. 200 m laterally and 200 m in depth, was sufficient such that the two wells did not stimulate the same volume of rock. While the positions of the NEF-1 and PNR-2_i faults overlap laterally, they are found at different depths, and do not overlap. They have near-orthogonal orientations.

The spatio-temporal evolution of the microseismicity during each stage follows a relationship of $r \propto t^{0.5}$. This is indicative of a process that is driven by diffusion of a pore pressure pulse from the injection point. This contrasts with the evolution of the PNR-1 microseismicity, where occurrence of seismicity was near-instantaneous at a range of distances, indicating a process driven by poro-elastic stress transfer. This serves to demonstrate that a range of mechanisms can act to reactivate faults during hydraulic fracturing, and that in some cases, several mechanisms may act in tandem. Modelling of the stress transfer produced by tensile hydraulic fracture opening shows that this would also have moved the PNR-2_i fault closer to failure as well. The diffusion-dominated process, and the distance of the PNR-2_i fault from the well, produced a delay between injection and fault reactivation, such that the injection stages were completed before any substantial fault reactivation was observed.

Finally, we investigated potential reasons for the difference in the levels of fault reactivation between the PNR-1z and PNR-2 wells. The NEF-1 fault appears to be a larger structure, and received a larger volume of injected fluid, however the seismicity it produced was an order of magnitude smaller than the PNR-2_i fault, which is a smaller structure, and it received a lower volume of injected fluid. We found that the NEF-1 fault is moderately well orientated in the *in situ* stress field, such that a substantial perturbation was required for reactivation. In contrast, the PNR-2_i fault is extremely well orientated in the stress field, such that it was likely at, or very close to, its critical stress state, such that a very small perturbation was sufficient to produce seismicity. These observations demonstrate the importance of the *in situ* stress state, and the orientations of faults within the stress field, in determining the rates and magnitudes of seismicity that result during hydraulic fracturing.

REFERENCES

Abercrombie R.E., 1995. Earthquake source scaling relationships from –1 to 5 M_L using seismograms recorded at 2.5-km depth: Journal of Geophysical Research 100, 24015-24036.

Aki K. 1965. Maximum likelihood estimate of b in the formula log N = a-bM and its confidence: Bulletin of the Earthquake Research Institute 43: 237-239.

Aki K., 1966. Generation and propagation of G waves from the Niigata earthquake of June 14, 1964. Part 2. Estimation of earthquake moment, released energy and stress-strain drop from G wave spectrum: Bulletin of the Earthquake Research Institute, 44: 73-88.

Bao X. and D.W. Eaton, 2016. Fault activation by hydraulic fracturing in Western Canada: Science 354, 1406-1409.

Butcher A., R. Luckett, J.P. Verdon, J-M. Kendall, B. Baptie, J. Wookey, 2017. Local magnitude discrepancies for near-event receivers; implications for the UK traffic light scheme: Bulletin of the Seismological Society of America 107, 532-541.

Butcher A., R. Luckett, J-M. Kendall, B. Baptie, 2020. Seismic magnitudes, corner frequencies and microseismicity: using ambient noise to correct for high-frequency attenuation: Bulletin of the Seismological Society of America 110, 1260-1275.

Clarke H., P. Turner, R.M. Bustin, N. Riley, B. Besly, 2018. Shale gas resources of the Bowland Basin, NW England: a holistic study: Petroleum Geoscience 24, 287-322.

Clarke H., J.P. Verdon, T. Kettlety, A.F. Baird, J-M. Kendall, 2019a. Real time imaging, forecasting, and management of human-induced seismicity at Preston New Road, Lancashire, England: Seismological Research Letters 90, 1902-1915.

Clarke H., H. Soroush, T. Wood, 2019b. Preston New Road: the role of geomechanics in successful drilling of the UK's first horizontal shale gas well: Society of Petroleum Engineers EUROPEC at the 81st EAGE Annual Conference, SPE-195563.

Clauset A., C.R. Shalizi, M.E.J. Newman, 2009. Power-law distributions in empirical data: Society of Industrial and Applied Mathematics Reviews: 51, 661-703.

Cuadrilla Resources, 2019. Hydarulic Fracture Plan PNR 2. Available at: https://consult.environment-agency.gov.uk/onshore-oil-and-gas/information-on-cuadrillas-preston-new-road-site/user_uploads/pnr-2-hfp-v3.0.pdf (last accessed, 25/02/2020).

Deng K., Y. Liu, R.M. Harrington, 2016. Poroelastic stress triggering of the December 2013 Crooked Lake, Alberta, induced seismicity sequence: Geophysical Research Letters 43, 8482-8491.

Deichmann N., 2006. Local magnitude, a moment revisited: Bulletin of the Seismological Society of America 96, 1267-1277.

Dohmen T., J. Zhang, J.P. Blangy, 2014. Measurement and analysis of 3D stress shadowing related to the spacing of hydraulic fracturing in unconventional reservoirs: Society of Petroleum Engineers Annual Conference, Amsterdam, SPE-170924.

Eaton D.W., 2018. Passive seismic monitoring of induced seismicity: Cambridge University Press.

Eyre T.S., D.W. Eaton, M. Zecevic, D. D'Amico, D. Kolos, 2019. Microseismicity reveals fault activation before M_W 4.1 hydraulic-fracturing induced earthquake: Geophysical Journal International 218, 534-546.

Frohlich C. and S.D. Davis, 1993. Teleseismic b values; or, much ado about 1.0: Journal of Geophysical Research 98, 631-644.

Galis M., J.P. Ampuero, P.M. Mai, F. Cappa, 2017. Induced seismicity provides insight into why earthquake ruptures stop: Science Advances 3, eaap7528.

Ghanizadeh A., C. Clarkson, S. Aquino, O.H. Ardakani, H. Sanei, 2015. Petrophysical and geomechanical characteristics of Canadian tight oil and liquid-rich gas reservoirs: I. Pore network and permeability characterization: Fuel 153, 664-681.

Gholipour A.M., J.W. Cosgrove, M. Ala, 2016. New theoretical model for predicting and modelling fractures in folder fractured reservoirs: Petroleum Geoscience 22, 257-280.

Gischig V.S., 2015. Rupture propagation behavior and the largest possible earthquake induced by fluid injection into deep reservoirs: Geophysical Research Letters 42, 7420-7428.

Green R.G., T. Greenfield, R.S. White, 2015. Triggered earthquakes suppressed by an evolving stress shadow from a propagating dyke: Nature Geoscience 8, 629-633.

Gutenberg B., and C. F. Richter, 1944. Frequency of earthquakes in California: Bulletin of the Seismological Society of America 34, 185-188.

Haimson B. and C. Fairhurst, 1967. Initiation and extension of hydraulic fractures in rocks: Society of Petroleum Engineers 3rd Conference on Rock Mechanics, Austin, SPE-1710.

Hallo M., I. Oprsal, L. Eisner, M.Y. Ali, 2014. Prediction of magnitude of the largest potentially induced seismic event: Journal of Seismology 18, 421-431.

Hanks T.C. and H. Kanamori, 1979. A moment magnitude scale: Journal of Geophysical Research 84, 2348-2350.

Holland A.A., 2013. Earthquakes triggered by hydraulic fracturing in south-central Oklahoma: Bulletin of the Seismological Society of America 103, 1784-1792.

Huang B. and J. Liu, 2017. Experimental investigation of the effect of bedding planes on hydraulic fracturing under true triaxial stress: Rock Mechanics and Rock Engineering 50, 2627-2643.

Kanamori H. and E.E. Brodsky, 2004. The physics of earthquakes: Reports on Progress in Physics 67, 1429-1496.

Kettlety T., J.P. Verdon, M.J. Werner, J-M. Kendall, J. Budge, 2019. Investigating the role of elastostatic stress transfer during hydraulic fracturing-induced fault reactivation: Geophysical Journal International 217, 1200-1216.

Kettlety T., J.P. Verdon, M. Werner, J-M. Kendall, 2020. Stress transfer from opening hydraulic fractures controls the distribution of induced seismicity: Journal of Geophysical Research 125, e2019JB018794.

Kwiatek G., T. Saamo, T. Ader, F. Bluemle, M. Bohnhoff, M. Chendorain, G. Dresen, P. Heikkinen, I. Kukkonen, P. Leary, M. Leonhardt, P. Malin, P. Martínez-Garzón, K. Passmore, P. Passmore, S. Valenzuela, C. Wollin, 2019. Controlling fluid-induced seismicity during a 6.1-km-deep geothermal stimulation in Finland: Science Advances 5, eaav7224.

Liu H., X. Hu, Y. Guo, X. Ma, F. Wang, Q. Chen, 2019. Fracture characterization using flowback water transients from hydraulically fractured shale gas wells: ACS Omega 4, 14688-14698.

Luckett R., L. Ottemöller, A. Butcher, B. Baptie, 2019. Extending local magnitude M_L to short distances: Geophysical Journal International 216, 1145-1156.

Maxwell S.C., J. Shemeta, E. Campbell, D. Quirk, 2008. Microseismic deformation rate monitoring: SPE Annual Technical Conference, SPE116596.

Maxwell S.C., M. Jones, R. Parker, S. Miong, S. Leaney, D. Dorval, D. D'Amico, J. Logel, E. Anderson, K. Hammermaster, 2009. Fault activation during hydraulic fracturing: SEG Annual Meeting Expanded Abstracts 28, 1552-1556.

Nagel N.B. and M. Sanchez-Nagel, 2011. Stress shadowing and microseismic events: a numerical evaluation: Society of Petroleum Engineers Annual Conference, Denver, SPE-147363.

Okada Y., 1992. Internal deformation due to shear and tensile faults in a half-space: Bulletin of the Seismological Society of America 82, 1018-1040.

Peacock D.C.P., C.W. Nixon, A. Rotevatn, D.J. Sanderson, L.F. Zuluaga, 2016. Glossary of fault and other fracture networks: Journal of Structural Geology 92, 12-29.

Questiaux J-M., G.D. Couples, N. Ruby, 2010. Fractured reservoirs with fracture corridors: Geophysical Prospecting 58, 279-295.

Rice J.R. and M.P. Cleary, 1976. Some basic stress diffusion solutions for fluid-saturated elastic porous media with compressible constituents: Reviews of Geophysics and Space Physics 14, 227-241.

Rogers S.F., 2003. Critical stress-related permeability in fractured rocks, in M. Ameen (ed.), Fracture and In Situ Stress Characterisation of Hydrocarbon Reservoirs, Geological Society of London Special Publication 209, 7-16.

Schlaphorst D., J-M. Kendall, J. Collier, J.P. Verdon, J. Blundy, B.J. Baptie, J. Latchman, F. Massin, M-P. Bouin, 2016. Water, oceanic fracture zones and the lubrication of subducting plate boundaries - insights from seismicity: Geophysical Journal International 204, 1405-1420.

Scholz C.H., 1968. The frequency-magnitude relation of microfracturing in rock and its relation to earthquakes: Bulletin of the Seismological Society of America 58, 399-415.

Schultz R., V. Stern, M. Novakovic, G. Atkinson, Y.J. Gu, 2015. Hydraulic fracturing and the Crooked Lake sequences: Insights gleaned from regional seismic networks: Geophysical Research Letters 42, 2750-2758.

Shapiro S.A., 2008. Microseismicity: A Tool for Reservoir Characterization: EAGE Publications.

Shapiro S.A. and C. Dinske, 2009. Fluid-induced seismicity: pressure diffusion and hydraulic fracturing: Geophysical Prospecting 57, 301-310.

Shapiro S.A., E. Huenges, G. Borm, 1997. Estimating the crust permeability from fluid-injection-induced seismic emission at the KTB site: Geophysical Journal International 131, F15-F18.

Shapiro S.A., C. Dinske, E. Rothert, 2006. Hydraulic-fracturing controlled dynamics of microseismic clouds: Geophysical Research Letters, 33, L14312.

Shapiro S.A., C. Dinske, C. Langenbruch, 2010. Seismogenic index and magnitude probability of earthquakes induced during reservoir fluid stimulations: The Leading Edge 29, 304-309.

Stein R.S., 1999. The role of stress transfer in earthquake occurrence: Nature 402, 605-609.

Toda S., R.S. Stein, T. Sagiya, 2002. Evidence from the AD 2000 Izu islands earthquake swarm that stressing rate governs seismicity: Nature 419, 58-61.

Verdon J.P., and J. Budge, 2018. Examining the capability of statistical models to mitigate induced seismicity during hydraulic fracturing of shale gas reservoirs: Bulletin of the Seismological Society of America 108, 690-701.

Verdon J.P., A. Wuestefeld, J.T. Rutledge, I.G. Main, J.M. Kendall, 2013. Correlation between spatial and magnitude distributions of microearthquakes during hydraulic fracture stimulation: 75th EAGE Annual Conference, Expanded Abstracts Th 01 12.

Verdon J.P., T. Kettlety, J-M. Kendall, 2019a. Geomechanical interpretation of microseismicity at the Preston New Road PNR-1z well, Lancashire, England: Report commissioned by the Oil and Gas Authority, OLG.OGA-PNR2.

Verdon J.P., N. Igonin, M. Kendall, D. Eaton, 2019b. Fault reactivation via pre-existing fracture networks during hydraulic fracturing: Society for Earthquake and Civil Engineering Dynamics (SECED) Conference Proceedings, Greenwich, Abstract No. 7.4.

Walsh F.R. and M.D. Zoback, 2016. Probabilistic assessment of potential fault slip related to injection-induced earthquakes: application to north-central Oklahoma, USA: Geology 44, 991-994.

Wang R., F Lorenzo-Martin, F. Roth, 2006. PSGRN/PSCMP – a new code for calculating co- and post-seismic deformation, geoid and gravity changes based on the viscoelastic-gravitational dislocation theory: Computers and Geosciences 32, 527-541.

Wyss M., K. Shimazaki, S. Wiemer, 1997. Mapping active magma chambers by b values beneath the off-Ito volcano, Japan: Journal of Geophysical Research 102, 20413-20422.

OUTER LIMITS